4

UED METHODOLOGY*

4.1 Introduction

The total temporal resolution of UED, Δt_{total}, depends on the durations of the pump pulse ($\Delta t_{\text{p-laser}}$) and electron pulses ($\Delta t_{\text{electron}}$) and on temporal broadening caused by velocity mismatch between photons and electrons (Δt_{VM}):

$$\Delta t_{\text{total}}^2 = \Delta t_{\text{p-laser}}^2 + \Delta t_{\text{electron}}^2 + \Delta t_{\text{VM}}^2 \tag{4–1}$$

---

[*] Parts of this chapter have been adapted from Srinivasan, R.; Lobastov, V.A.; Ruan, C.-Y.; Zewail, A.H., *Helv. Chim. Acta*, **2003**, *86*, 1762.

Eqn. 4–1 is based on the assumption that the laser and electron beams have Gaussian spatial and temporal profiles and that the density profile of the molecular beam cross-section is Gaussian. The fwhm of the pump laser pulse ($\Delta t_{\text{p-laser}}$) is 120 fs, which is smaller than the contributions from the other two terms. Consequently, the laser pulse contribution to the total experimental temporal resolution is relatively small, and this section will focus primarily on the duration of the electron pulse and the impact of velocity mismatch.

4.2 Streaking: Electron Pulse Characterization

Several different factors contribute to temporal broadening in the formation of short electron pulses, and these factors have been extensively examined in the streak camera literature. The total streak camera resolution, Δt_{R}, is often defined as a function of three different pulse-broadening sources:[1]

$$\Delta t_{\text{R}}^2 = \Delta t_{\text{e-laser}}^2 + \Delta t_{\text{D}}^2 + \Delta t_{\text{S}}^2 \tag{4–2}$$

where $\Delta t_{\text{e-laser}}$ is the temporal duration of the laser pulse, which creates the photoelectrons, Δt_{D} is the broadening of the electron pulse from its generation until it strikes the detector, and Δt_{S} is related to the detector geometry and spatial resolution. Eqn. 4–2 is based on the assumption that the electron pulses have a Gaussian temporal distribution. The first term of Eqn. 4–2 corresponds to the temporal fwhm of the laser pulse, in this case 120 fs. The second term in Eqn. 4–2, Δt_{D}, represents broadening of the electron pulse as it travels from the photocathode to the detector. The broadening of the electron pulse can be classified into three regimes: initial broadening at the photocathode caused by the angular and energetic spread of the ejected photo-electrons; subsequent broadening of the pulse in the region of high electron density between the photocathode and anode due to space–charge effects; and broadening over the rest of the travel distance mainly due to non-uniform electron velocity distribution. For our current time resolution of 1 ps, the initial temporal broadening and the space–charge effects dominate the pulse broadening.

The initial temporal broadening of the photoelectrons is given by:[1]

$$\Delta t_{\mathrm{D(initial)}} = \frac{\sqrt{2m_e \Delta\varepsilon}}{eE_{\mathrm{PC}}} \tag{4–3}$$

where $\Delta\varepsilon$ is the fwhm of the ejected photoelectron energy distribution, e is the electron charge, m_e is the electron mass, and E_{PC} is the electric field near the photocathode. Both E_{PC} and $\Delta\varepsilon$ may be controlled experimentally. The energy distribution, $\Delta\varepsilon$, which is related to the amount of excess energy in the photoemission process, can be minimized by proper selection of the photocathode material (hence its work function) and the incident laser wavelength. We have chosen to work with thin (*ca.* 450 Å) silver photocathodes, which have proved durable under our operating conditions and are easy to prepare. With a work function of 3.65 eV reported for a 450-Å Ag film, barring thermal effects and surface contamination, the photoelectron energy distribution is expected to be narrow (*ca.* 0.6 eV for a one-photon and *ca.* 2.5 eV for a two-photon emission process); note that the energy distribution of the laser pulse is only ~0.1 eV. Eqn. 4–3 shows that the initial temporal broadening also depends on the electric field E_{PC} between the photocathode and the extraction mesh. Our present electron gun design sets E_{PC} = 6 kV/ mm, which is similar to that used in state-of-the-art streak cameras. Under these conditions, we estimate $\Delta t_{\mathrm{D(initial)}}$ to be *ca.* 350 to 900 fs.

Once the electrons are extracted, the pulse undergoes collimation and deflection until it strikes the detector. From the instant the electrons are generated, electron–electron Coulombic repulsion causes pulse broadening, and the effects of this repulsion on the spatial and temporal characteristics of an electron pulse have been collectively called the space–charge effect. The influence of space–charge effects on temporal broadening can be understood by considering electrons at the front and back of an electron pulse. The front electrons are accelerated forward by repulsion from the electrons behind them, while the trailing electrons are decelerated by the charges in front. The net result is that the entire pulse broadens in all directions over time. Due to the inverse-square dependence of Coulombic repulsion on distance, space–charge effects are very sensitive to the electron density of the pulse and are greatly reduced when the electron density is low. One method for reducing the broadening is to accelerate the electrons to a high velocity within a very short distance; not only does this spread the electron pulse out over a greater distance, but it also reduces the time during which the electron pulse may broaden before intersecting the molecular beam or striking the detector. To reach sub-picosecond performance, the electron density must be reduced by limiting the number of electrons per pulse, which means that successful electron diffraction experiments require a high quantum efficiency detector such as a specially designed CCD camera.

The third term in Eqn. 4–2, Δt_S, contains broadening effects due to the detector. This *does not* reflect the temporal response of the detector itself, but rather how the spatial resolution and the position of the detector (with respect to the electron gun) influence streak measurements. When recording electron diffraction patterns, the electrons are not streaked, and, therefore, Δt_S does not apply to the UED experimental time resolution. We must, however, consider Δt_S when conducting streak experiments to measure the electron pulse length.

In the measurement of electron-pulse durations with streaking techniques, a time-dependent electric field is ramped across the first deflector pair such that an electron pulse traveling between the plates experiences a dispersive effect (Fig. 4–1). Very fast rates of voltage change ($\partial V/\partial t$) are required to disperse single picosecond pulses. To synchronize the arrival of the electron pulse with the maximum voltage gradient ($\partial V/\partial t$) at the streaking plates, an optical delay line was constructed to control the firing time of the photoconductive switch. Of the two optical arms, one is directed toward the switch and the other toward the photocathode on the electron gun. The arm leading to the electron gun incorporates a Michelson interferometer to generate laser pulse pairs with a well-defined pulse separation Δt_{sp}; Δt_{sp} is adjusted with a second optical delay. This laser pulse pair generates a pair of electron pulses with the same time separation Δt_{sp} at the photocathode.

After streaking, the two electron pulses are separated by a distance D_{pix} (in pixels) on the CCD detector. The streak velocity, in pixels per ps, is calculated from Δt_{sp} and D_{pix}. Single-shot streak image pairs are typically taken for a wide range of laser intensities in order to observe the effect of current density on the electron pulse length. By measuring the center position of each electron pulse on the CCD, the streak speed is readily calculated in units of pixels per picosecond. The pulse width of each electron pulse is then calculated by dividing the spatial fwhm of the pulse (pix) by the streak speed (pix/s).

The unstreaked electron beam profile is shown in Fig. 4–2, while a typical set of low-intensity electron pulse pairs obtained in UED-3 is shown in Fig. 4–3. After analyzing such pulse pairs, we obtain a curve that describes the temporal behavior of the electron gun as a function of the number of generated electrons (Fig. 4–4). It is clear from this curve that there is little or no broadening by space–charge effects at low numbers of electrons. Moreover, Fig. 4–5 also highlights the dramatic improvement in the electron gun performance in UED-3 as compared to UED-2—a 5-ps pulse in UED-2 contained only 3000 electrons, while in UED-3, an electron pulse of the same width contains nearly 100,000 electrons. The remarkable stability of the electron gun from pulse-to-pulse is depicted in Fig. 4–6, with measurements made on both sides of the detector.

4.3 Clocking: Zero of Time

In a UED experiment, the time coordinate for a reaction can only be established if there is a point of reference for the relative time delay between the initiation pulse and the electron pulse. This reference point is called time-zero (t_0), the time when both pulses simultaneously intersect in the sample. Careful measurement of laser and electron beam paths can narrow the time-zero window to within 100 ps. Another approach is to rely on the changes in the diffraction pattern of the system under investigation, but this is not an independent means of finding t_0. More importantly, this method is simply not practical for gas-phase work because of the long integration times required to obtain a single data point.

In the clocking technique developed for UED,[1] we use the crossed-beam geometry of the actual diffraction experiment to determine time-zero via the ‘lensing effect’. During CF_3I dissociation reaction studies, a dramatic change had been observed in the undiffracted electron beam profile when the excitation laser was present. The beam spot intensified along one axis, with a corresponding subtle decrease in the overall width (see Fig. 4–7). This effect only occurred when both the excitation laser and the molecular beam were present. The intensified strip was parallel to the laser axis and could be shifted up and down within the beam spot by adjusting the vertical tilt of the excitation laser entrance lens. Defocusing the laser reduced the stripe intensity. This phenomenon was termed photoionization-induced lensing. The effect is analogous to plasma lensing, a technique in which the high-energy charged beams in particle accelerators are focused by passing through a plasma field.

In our experiment, the pump laser photoionizes a fraction of the molecular beam sample, producing a mixture of positive ions and ejected electrons. The ejected electrons have an excess kinetic energy KE of

$$\mathrm{KE} = nhv - \Phi_{\mathrm{IP}} \tag{4–4}$$

where n is the number of photons involved in the excitation, v is the photon frequency, and Φ_{IP} is the ionization potential of the molecules. These ejected electrons begin to diffuse with their excess kinetic energy, resulting in net charge redistribution within the plasma. The ions remain more or less stationary on the picosecond time scale, so the net effect is the formation of a cylindrically symmetric charge gradient and a radial electric field about the initiation laser axis that focuses the charged electron beam. With less than 1% ionization, the radial electric field in the interaction region may be as high as 10 kV/m, which is sufficient to perturb the path of the incoming high-energy electron beam, and the effects are seen directly in the beam spot profile.

We exploited this phenomenon to obtain the time-zero for UED experiments. Time-resolved studies of photoionization-induced lensing were conducted on CF_3I gas, which has an ionization energy of 10.23 eV. For a three-photon process with 4.66-eV photons, the excess kinetic energy of the ejected electrons is *ca.* 3.7 eV, which corresponds to the electrons traveling *ca.* 1 μm in 1 ps. Fig. 4–8 shows the degree of lensing *vs.* time; the lensing is a maximum when the focused laser and electron pulses are temporally overlapped. The time at which the ellipticity of the electron beam begins to deviate from that of a symmetric profile is defined to be the reaction zero-of-time. The results elucidate t_0 precisely and, hence, allow a direct clocking of changes in the diffraction experiment with picosecond or shorter resolution.

4.4 Temporal and Spatial Overlap: Velocity Mismatch

The velocity of 30-keV electrons is approximately one-third the speed of light. This velocity mismatch causes different molecules across the laser-electron intersection region to experience different time delays between the two pulses. For example, if the laser pulse and the electron pulse copropagate, and if both reach the near edge of the molecular beam at the same instant, then the electron beam (on account of its lower velocity) will encounter molecules at the farther edge of the sample at much later times after the light pulse has passed through. Since the time required for the electrons to cross the molecular beam sample is on the order of picoseconds, the temporal broadening due to velocity mismatch is a significant contributor to the total experimental resolution. In principle, temporal broadening due to velocity mismatch might be large enough that the total experimental resolution does not improve when shorter electron pulses or shorter laser pulses are introduced. To estimate the importance of velocity mismatch, we used a geometrical model[1] to represent the temporal broadening with an analytical function in terms of experimental parameters (Fig. 4–9).

Our theoretical model of velocity mismatch encompasses several factors: (1) the ratio of the photon velocity to the electron velocity, κ; (2) the spatial fwhm of the laser pulse, w_L; (3) the spatial fwhm of the electron pulse, w_e; (4) the cross-sectional fwhm of the molecular beam, w_M; (5) the angle of intersection θ between the laser pulse and the electron pulse. When the two beams copropagate, the fwhm of the temporal broadening is given by:

$$\Delta t_{\mathrm{VM}}(\theta=0)=\frac{w_{\mathrm{M}}(\kappa-1)}{c} \qquad (4\text{–}5)$$

As expected, if the laser and electron pulses have identical velocities ($\kappa = 1$), and are co-propagating ($\theta = 0$), then there is no velocity mismatch. Note that thin molecular samples reduce Δt_{VM}, and there is negligible broadening when the electron velocity approaches the speed of light ($\kappa \to 1$).

If the spatial width of the laser pulse is sufficiently small relative to w_M:

$$w_\mathrm{L} \leq w_\mathrm{M}\sqrt{\kappa - 1} \tag{4–6}$$

then the minimum temporal broadening actually occurs at a nonzero angle, θ_min, where

$$\theta_\mathrm{min} = \arccos\left(\frac{w_\mathrm{L}^2 + w_\mathrm{M}^2}{\kappa w_\mathrm{M}^2}\right) \tag{4–7}$$

The temporal broadening at this angle is:

$$\Delta t_\mathrm{VM}\left(\theta_\mathrm{min}\right) = \frac{w_\mathrm{L}}{c}\sqrt{\frac{\left(\kappa^2 - 1\right) - \frac{w_\mathrm{L}^2}{w_\mathrm{M}^2}}{1 + \frac{w_\mathrm{L}^2}{w_\mathrm{M}^2}}} \approx \frac{w_\mathrm{L}}{c}\sqrt{\kappa^2 - 1} \tag{4–8}$$

which is independent of the spatial width of the electron pulse.

For our UED apparatus, $\kappa \approx 3$ and typical beam fwhm values are w_e = 350 μm and $w_\mathrm{L} = w_\mathrm{M}$ = 250 μm. Fig. 4–10 displays the dependence of Δt_VM on the laser–electron beam intersection angle, and it can be seen that temporal broadening is minimized when the electron and laser beams are nearly perpendicular. In this manner, the overall temporal resolution of the experiment (which includes contributions from the electron pulse width, the laser pulse width, and the group velocity mismatch) is calculated as a function of the electron beam parameters (Fig. 4–11). For an electron beam condition of 300-μm diameter, the overall temporal resolution increases to only 4 ps for a pulse of 3.5 ps. As is readily seen from Eqn. 4–8, velocity mismatch can be further reduced by decreasing the ratio of the beam velocities, κ, which in turn implies higher accelerating voltages to increase the velocity of electrons. A decrease in the laser beam and molecular beam widths and reducing the laser-electron intersection angle from the present 90° to $\theta_{\min}$ (60°) (Fig. 4–10) will also serve to reduce velocity mismatch.

4.5 Calibration of CCD Camera

Figures 4–12 and 4–13 show the calibration of the pixel size on the CCD camera based on measurement of the intensity distribution and the estimation of the edge spread function. The USAF-1951 resolution target is used for this purpose. The calibration of the Modulation Transfer Function of the intensified CCD system is shown in Fig. 4–14 while Fig. 4–15 displays the single-electron-event statistics on the detector.

4.6 CCD Image Processing

The digital nature of our data acquisition permits the use of a variety of powerful image processing techniques that aid in the isolation of molecular diffraction signals. At each given time delay between pump (laser) and probe (electron) pulses, a series of 2-D diffraction images ($\boldsymbol{A}_i$, $i = 1, 2, \ldots, n$) are acquired with the CCD camera (here, bold characters denote 2-D images). The first step in the image processing is to generate an averaged 2-D image, from which unwanted random events have been removed; such events may be caused, for example, by spontaneous emission and cosmic rays. The averaged image, $\overline{\boldsymbol{A}}'$, is created according to the iterative procedure described below (Fig. 4–16).

A key trait of our 2-D data is the accessibility of the individual pixels in the digitized images, which allows us to treat each pixel as an independent detector statistically characterized by its own mean intensity and standard deviation. For each $\boldsymbol{A}_i$, a corresponding binary "mask" image, $\boldsymbol{M}_i$, is created. For example, a given pixel with coordinates (x,y) in each $\boldsymbol{M}_i$ has a value of *one* if the corresponding pixel in the diffraction image $\boldsymbol{A}_i$ is valid (the conditions for validity are outlined below) or has a value of *zero* otherwise. We define $M_i(x,y)$ as that pixel in a given $\boldsymbol{M}_i$ with coordinates (x,y); initially, $M_i(x,y) = 1$ for all pixels in all n mask images.

In the first step of each processing loop, an average value for the signal intensity at each pixel, $\overline{A}(x,y)$, is obtained over the n raw diffraction images:

$$\overline{A}(x,y) = \frac{\sum_i^n M_i(x,y) \cdot A_i(x,y)}{\sum_i^n M_i(x,y)} \tag{4–9}$$

where $A_i(x,y)$ is the signal intensity for the pixel with coordinates (x,y) in the ith diffraction image ($\boldsymbol{A}_i$), and the sum $\sum_i^n M_i(x,y)$ gives the number of valid pixels over all $\boldsymbol{A}_i$ with coordinates (x,y). During this step $\overline{A}(x,y)$ and $\sigma(x,y)$ (the standard deviation of the averaged scattering intensity) are calculated for each pixel in the average image $\overline{\boldsymbol{A}}$. In order to remove the signal spikes from random events, each diffraction image $\boldsymbol{A}_i$ is then submitted to a pixel-by-pixel rejection criterion requiring that the value of given pixel $A_i(x,y)$ lies within four standard deviations of the average value for that pixel (i.e., that $\overline{A}(x,y) - 4\sigma(x,y) \leq A_i(x,y) \leq \overline{A}(x,y) + 4\sigma(x,y)$). If a given value for $A_i(x,y)$ does not meet this criterion, then this pixel is declared invalid, and the value of $M_i(x,y)$ in the corresponding mask image $\boldsymbol{M}_i$ is set to zero—thereby preventing this pixel from contributing to the averaged signal in the next processing loop. This cycle is typically repeated three times, with the $\overline{A}(x,y)$ values, $\sigma(x,y)$ values, and the $\boldsymbol{M}_i$ mask images updated after each cycle.

At the conclusion of the last cycle, the final 2-D binary mask ($\boldsymbol{M}'$) is generated. Pixels in $\boldsymbol{M}'$ corresponding to inactive regions of the CCD camera (and pixels manually removed due to systematic problems) are set to zero, thereby ensuring that these regions do not contribute to the final diffraction signal when the averaged $\overline{\boldsymbol{A}}$ image is multiplied by this final mask. This process yields the final, processed averaged image, $\overline{\boldsymbol{A}}'$, which is now used for all further analysis. All averaged images, including background images and the reference gas images, were generated by this procedure.

Next, an averaged background image ($\overline{\boldsymbol{B}}'$), obtained under identical conditions as the molecular diffraction image (e.g., exposure time, laser light scattering, etc.)—except *without* the presence of the gas sample under study—is then subtracted from $\overline{\boldsymbol{A}}'$. After this background subtraction, the 2-D diffraction image is then divided by a corresponding reference 2-D image, $\overline{\boldsymbol{X}}'$, obtained from a monatomic gas (xenon):

$$\boldsymbol{R}^{2D} = \frac{\overline{\boldsymbol{A}}' - \overline{\boldsymbol{B}}'}{\overline{\boldsymbol{X}}' - \overline{\boldsymbol{B}}_X{}'} \tag{4–10}$$

where $\overline{\boldsymbol{B}}_X{}'$ is the corresponding background image for $\overline{\boldsymbol{X}}'$. This division by the smoothly decaying diffraction intensity of the atomic reference gas not only permits the direct visualization of molecular interferences (rings) in the 2-D "ratio" images, $\boldsymbol{R}^{2D}$, but also removes most of the systematic errors associated with the apparatus function of the detector. Each $\boldsymbol{R}^{2D}$ is then converted to an experimental 1-D total intensity curve, $R^E(pix)$, by calculating the average intensity as a function of pixel radius, $\rho(pix)$, from the electron beam center, according to the relation:

$$\sqrt{x^2 + y^2} < \rho < \sqrt{(x+1)^2 + (y+1)^2} \qquad (4\text{–}11)$$

Corresponding values for the standard deviation of the scattering intensity at each pixel radius, $\sigma(pix)$, are also calculated, permitting an additional round of spike rejection in the final calculation of $R^E(pix)$. The $\sigma(pix)$ values are then used later as the weighting function in least-squares refinements (see below). Finally, $R^E(pix)$ is converted to $R^E(s)$ by calculating the scattering angle θ from the pixel dimensions and the camera length L (which is defined as the distance between the scattering volume beneath the sample nozzle and the detection screen). The camera length for these experiments was calibrated by comparing experimentally derived diffraction data obtained from high-purity nitrogen gas with literature values. The division by the reference gas scattering intensity is accounted for by multiplying $R^E(s)$ by the theoretical scattering intensity of the reference gas, $I^T_{ref}(s)$:

$$I^E(s) = R^E(s) \times I^T_{ref}(s) \qquad (4\text{–}12)$$

The experimental 1-D diffraction curves, $I^E(s)$, may then be analyzed to generate the $sM^E(s)$ and $f(r)$ curves that reflect the structural features of the molecules under study.

4.7 Normalization of Time-Dependent Diffraction Signals

Before analyzing time-dependent diffraction signals, we normalize the total intensity of each time-dependent 2-D image, $\overline{\mathbf{A}}'(t)$. This normalization procedure removes any systematic variation (~1% or less) in electron scattering intensity as a function of temporal delay (e.g., resulting from minuscule changes in photon flux at the photocathode as the delay line retroreflector is placed at different positions). The normalization is performed by first calculating the mean intensity of each image, $\langle \overline{\mathbf{A}}'(t) \rangle$, according to the relation:

$$\langle \overline{\mathbf{A}}'(t) \rangle = \frac{\sum_{x,y}^{512} M'(x,y;t) \cdot \overline{A}'(x,y;t)}{\sum_{x,y}^{512} M'(x,y;t)} \tag{4–13}$$

where $\overline{A}'(x,y;t)$ is the signal intensity at the pixel with coordinates (x,y) in the averaged 2-D image acquired at time delay t, $\mathbf{M}'(t)$ is the binary mask image corresponding to the diffraction image $\overline{\mathbf{A}}'(t)$, and 512 is the effective number of pixels along both x and y (our CCD camera has 1024×1024 pixels, but 2×2 binning is typically employed). The quantity $\langle \overline{A}'(t) \rangle^{-1}$ obtained at each time delay is then used as the normalization constant for the corresponding averaged 2-D image. Once normalization has been performed, the diffraction difference method can be employed.

4.8 Analysis of 1D Diffraction Data: Ground-State Structures

The procedure for processing our diffraction data is illustrated in Fig. 4–17. The experimental diffraction intensity curve is a sum of the desired structural information, $I_M^E(s)$, and a background intensity profile, $I_B^E(s)$:

$$I^E(s) = I_B^E(s) + I_M^E(s) \tag{4–14}$$

where $I_B^E(s)$ contains contributions from atomic scattering, $I_A(s)$, and the experimental background response. Thus, the modified experimental molecular scattering intensity is given by:

$$sM^E(s) = s\,\frac{I^E(s) - I_B{}^E(s)}{I_A(s)} \tag{4–15}$$

or

$$sM^{E}(s) = s\frac{I^{E}(s) - I_{B}{}^{E}(s)}{|f_a||f_b|} \tag{4–16}$$

We did not obtain the curve for $I_B{}^E(s)$ by merely calibrating the detector because the amount of scattered laser light and other factors varied from experiment to experiment and with each molecular system. Instead, background curves were independently estimated for each experiment. Such background curves may be ascertained using different methods, three of which are described: (1) A crude yet often effective approximation is a low-order polynomial curve fit through all the data points of $I^E(s)$; (2) A more rigorous way of obtaining $I_B{}^E(s)$ exploits the sinusoidal nature of $I_M(s)$, cycling above and below zero several times over the experimental detection range. This approach introduces a set of zero-positions, s_n, of s where the theoretical molecular intensity curve, $I_M{}^T(s)$, crosses zero: i.e, $I_M{}^T(s_n) = 0$. If $I_M{}^T(s)$ approaches $I_M{}^E(s)$, it should then hold from Eqn. 4–14 that $I^E(s_n) = I_B{}^E(s_n)$ at the zero-positions, s_n. Therefore, $I_B{}^E(s)$ can be approximated by fitting a polynomial curve through $[s_n, I^E(s_n)]$; (3) A third way to estimate $I_B{}^E(s)$ is to express $I_B{}^E(s)$ independently as a polynomial curve defined by the variable coefficients of each order, and to optimize these variables by minimizing the difference (more precisely, χ^2) between $I_M{}^T(s)$ and $I_M{}^E(s)$. This method should produce the same background curve obtained with the second method if there is no systematic error. These three methods can also be applied to the time-resolved diffraction data, as explained later.

4.9 Time-Resolved Experiments: The Diffraction-Difference Method

In order to follow the structural changes that occur over the course of a given chemical reaction, we recorded a series of averaged 2-D diffraction images with varying time delay, t, between the pump (laser) and probe (electron) pulses. Each of these images thus reflects the transient behavior of the molecular structures at the corresponding temporal delay following laser excitation. Unlike the ground-state data, the scattering intensity at a time $t > 0$, $I(t > 0; s)$ contains contributions from more than one type of molecular species—not just the parent molecules, but also intermediates and products of the reaction. Therefore, the time-resolved scattering intensity $I(t; s)$ can be written as a sum of the individual scattering intensities from each species at time t, $I_\alpha(t; s)$:

$$I(t;s) = \sum_{\alpha} I_\alpha(t;s) \tag{4–17}$$

where α indexes all possible structures occurring over the course of the reaction. If the molecular structures of the species formed (transient or otherwise) do not change significantly over the time window that defines the species α, we may partition the time dependence of $I_\alpha(t;\ s)$ into the relative concentration of structure α by writing:

$$I(t;s) = \sum_\alpha I_\alpha(t;s) \approx \sum_\alpha p_\alpha(t) \cdot I_\alpha(s) \tag{4–18}$$

where $p_\alpha(t)$ is the population (or mole fraction) of a given structure α and $I_\alpha(s)$ is the time *independent* scattering intensity from that structure. In the present case, we will consider α to refer to parent, intermediate, and product structures.

In UED, all species present will scatter the incident electrons regardless of their participation in the chemical reaction. Thus, in most cases the vast majority (>85–90%) of the diffracting media is comprised of non-reacting parent molecules: $p_{\text{parent}} >> p_{\text{intermediate}}$ or p_{product}. Furthermore, the molecular scattering intensity from a reaction fragment is usually weaker than that from a parent molecule because it has fewer internuclear pairs. Therefore, in order to accentuate the diffraction signal arising from structural changes occurring over the course of the reaction, we employed the so-called diffraction-difference method (Fig. 4–18), whereby we use a reference image to obtain the diffraction-difference signal, $\Delta I(t;\ t_{\text{ref}};\ s)$, from the relation:

$$\Delta I(t;\, t_{\text{ref}};\, s) = I(t;\, s) - I(t_{\text{ref}};\, s) \tag{4–19}$$

where t_{ref} refers to the reference time (e.g., prior to the arrival of the reaction-initiating laser pulse). Combining Eqns. 4–18 and 4–19 gives:

$$\Delta I(t;\, t_{\text{ref}};\, s) \approx \sum_{\alpha} p_{\alpha}(t) \cdot I_{\alpha}(s) - \sum_{\alpha} p_{\alpha}(t_{\text{ref}}) \cdot I_{\alpha}(s) = \sum_{\alpha} \Delta p_{\alpha}(t; t_{\text{ref}}) \cdot I_{\alpha}(s) \tag{4–20}$$

Equation (4–20) thus presents $\Delta I(t;\, t_{\text{ref}};\, s)$ in terms of the *changing populations* of the molecular structures involved—if the molecular structure of a given species *does* undergo significant structural change during the time window of the experiment, it may be necessary to refine its structural parameters at each point in time.

The diffraction-difference method has several general advantages. First, the large (unwanted) background signal from atomic scattering is a common contribution to all images—regardless of the temporal delay and the nature of the reaction—and can, therefore, be essentially removed by the subtraction. It follows from the definition of the total scattering intensity, I^E ($= I_{\text{M}}^E + I_{\text{B}}^E$), that the experimental difference curve is given by:

$$\Delta I^E(t;\, t_{\text{ref}};\, s) = \Delta I_{\text{M}}^E(t;\, t_{\text{ref}};\, s) + \Delta I_{\text{B}}^E(t;\, t_{\text{ref}};\, s) \tag{4–21}$$

Because $I_B{}^E$ is comprised mostly of atomic scattering, which is unchanged over the course of a chemical reaction, $\Delta I_B{}^E(t;\ t_{\mathrm{ref}};\ s)$ should be nearly zero. Thus, whereas the total diffraction signal, $I(t;\ s)$, is dominated by the background intensity, $I_B{}^E(t;\ s)$, the diffraction-difference curve is dominated by the molecular scattering intensity, $I_M{}^E(t;\ s)$:

$$\Delta I^E(t;\ t_{\mathrm{ref}};\ s) \approx \Delta I_M{}^E(t;\ t_{\mathrm{ref}};\ s) \qquad (4\text{–}22)$$

Second, any intrinsic systematic error of the detection system will be greatly reduced (or effectively eliminated) by the subtraction. Third, each diffraction-difference curve reflects comparable contributions from the parent and product structures—in contrast to the original raw data, wherein only a relatively small fraction of the signal comes from products (and/or intermediates), with the vast majority of the signal originating from the parent. Therefore, the significance of the product contribution is dramatically enhanced in $\Delta I(t;\ t_{\mathrm{ref}};\ s)$: $|\Delta p_{\mathrm{parent}}| \approx |\Delta p_{\mathrm{intermediate}}| \approx |\Delta p_{\mathrm{product}}|$ (Note that the diffraction-difference method does not depend on the specific formulae used to express I_M).

If desired, knowledge of the fractional changes of the species involved in the reaction, $\Delta p_\alpha\ (t;\ t_{\mathrm{ref}})$, can be used to extract the molecular diffraction signal resulting only from the reaction's products. The parent diffraction signal ($I_{parent}(s)$, obtained at a negative time) is scaled by $\Delta p_{parent}(t;\ t_{\mathrm{ref}})$ and added to the diffraction difference signals obtained at positive times, thereby canceling out the parent contribution:

$$\Delta I(t;t_{\mathrm{ref}};s) - \Delta p_{parent}(t;t_{\mathrm{ref}}) \cdot I_{parent}(s) = \sum_{\alpha \neq parent} \Delta p_{\alpha}(t;t_{\mathrm{ref}}) \cdot I_{\alpha}(s) \tag{4–23}$$

(Note that $\Delta\, p_{\alpha}\,(t;\ t_{\mathrm{ref}})$ is typically a negative number). This procedure, which we have referred to as the "product-isolated" or "product-only" method, has been utilized frequently in our more recent work.

Prior to analyzing the diffraction-difference signals, high-frequency noise was reduced with low-pass Fourier filtering (performed via convolution with a parabolic cut-off function valued 1.0 at 0.0 Å and 0.0 at ≈8.7 Å). This filter, which was carefully chosen to prevent any significant damping of higher-frequency components of the diffraction signal, reduced the standard deviation values resulting from least-squares fitting by about half compared to similar analyses of unfiltered data but did not significantly alter the results of the fits.

4.10 Least-Squares Fitting

Refinements of the diffraction data were performed with software developed in-house using a procedure (similar to that used in conventional gas-phase electron diffraction) that iteratively minimizes the statistical χ^2. For example, for a given difference curve, $\Delta I^{E}(t;\ t_{\mathrm{ref}};\ s)$, the determination of the relative fractions or structural parameters of each molecular species was made by minimizing:

$$\chi^2 = \sum_{s_{\min}}^{s_{\max}} \frac{[S_c \cdot \Delta sM^T(t;t_{ref};s) - \Delta sM^E(t;t_{ref};s)]^2}{[\sigma(s)]^2} \tag{4–24}$$

where the $\Delta sM(s)$ is the difference modified molecular scattering intensity, $\sigma(s)$ is the standard deviation of $\Delta sM^E(t;\, t_{\mathrm{ref}};\, s)$ at each s position (over the available range), and S_c is a scaling factor (whose magnitude is determined by the amplitude of the ground-state signal). $\Delta sM^E(t;\, t_{\mathrm{ref}};\, s)$ is obtained from $\Delta I^E(t;\, t_{\mathrm{ref}};\, s)$, and the $\sigma(s)$ values are calculated from the corresponding values of $\sigma(pix)$ (the standard deviation of the scattering intensity at each pixel radius) with appropriate error propagation.

Beginning with an assumed initial product distribution and the starting structural parameters for each species, the software first fits the residual background, $\Delta I_{\mathrm{B}}{}^E(t;\, t_{\mathrm{ref}};\, s)$, with the experimental $\Delta I^E(t;\, t_{\mathrm{ref}};\, s)$ values at the zero-positions (s_n) of the theoretical $\Delta I_{\mathrm{M}}{}^T(t;\, t_{\mathrm{ref}};\, s)$ curve. Then the experimental $\Delta sM^E(t;\, t_{\mathrm{ref}};\, s)$ curve is obtained with the background-free ΔI, and χ^2 is calculated to evaluate the quality of the fit. This procedure is repeated until the best least-squares fit between theoretical and experimental $\Delta sM(s)$ curves is reached (i.e, until χ^2 is minimized). In the fitting algorithm, the absolute amplitude of the diffraction-difference signal may then be scaled to that of the ground-state signal to give the relative number densities of every structure at each time delay over the course of the experiment.

4.11 Estimation of Spatial Coherence

The primary purpose of the electron beam being to record diffraction images, the electron beam has to maintain spatial as well as temporal coherence. Spatial coherence describes the phase correlation between different points in the electron beam; if phase correlation is lost over a distance X, then two atoms separated by X will not contribute interference terms to the scattered intensity. Estimates of coherence are estimated below for transverse (lateral) dimensions and longitudinal (chromatic) dimensions. The lateral coherence length, X_L, for a circular, uniform, and monochromatic source is calculated from:

$$X_L = \lambda/\alpha \tag{4–25}$$

where α is the angular divergence of the beam.

In order to measure the divergence of the electron beam in UED-3, we measured the size of the electron beam at the detector. We also measured the edge spread function of the e-beam at an earlier position along its trajectory by using a knife edge. The edge spread function was measured by introducing a secondary Al target into the path of the e-beam at a distance of L = 143 mm from the phosphor screen and with steps of 0.125 mm. The resultant integral intensity measured on the screen is plotted against the position of the Al edge, as shown in Fig. 4–19. Using the geometrical constraints as depicted in the figure, the divergence of our electron beam has been estimated to be 0.35 mrad. Using the relativistic wavelength for 30 keV electrons, the lateral coherence length of the UED-3 electron beam is estimated to be 100 Å. Non-monochromaticity corrections have not been included in this estimation.

References

1. Williamson, J. C. Ultrafast Gas-Phase Electron Diffraction. Ph.D. Thesis, California Institute of Technology, Pasadena, 1998.

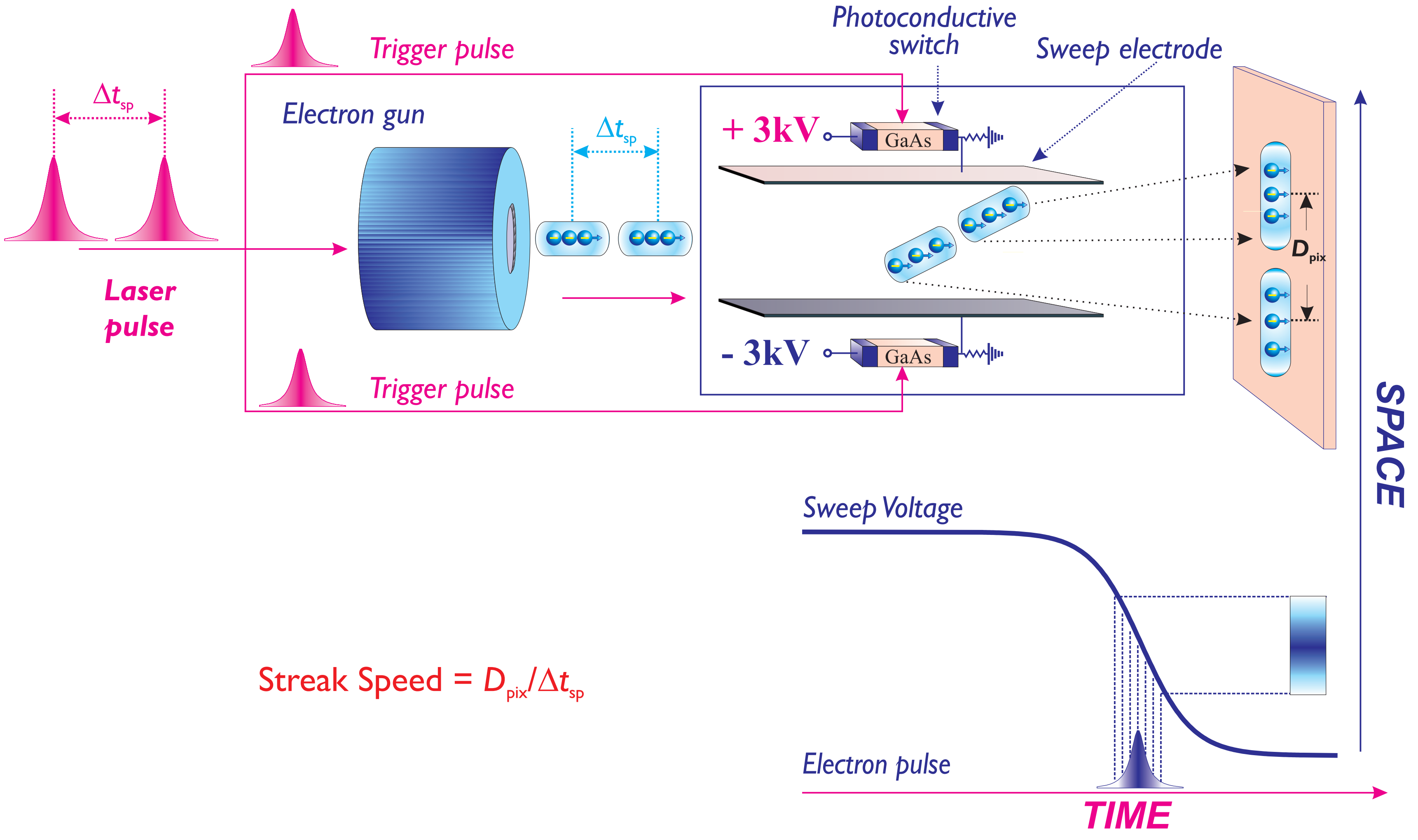

Figure 4-1. Calibration of electron gun via streaking experiments. Two electrons separated in time by Δt_{sp} enter a pair of streak plates. A fast voltage gradient across the streak plates causes the electrons to be separated by a distance D_{pix} at the detector.

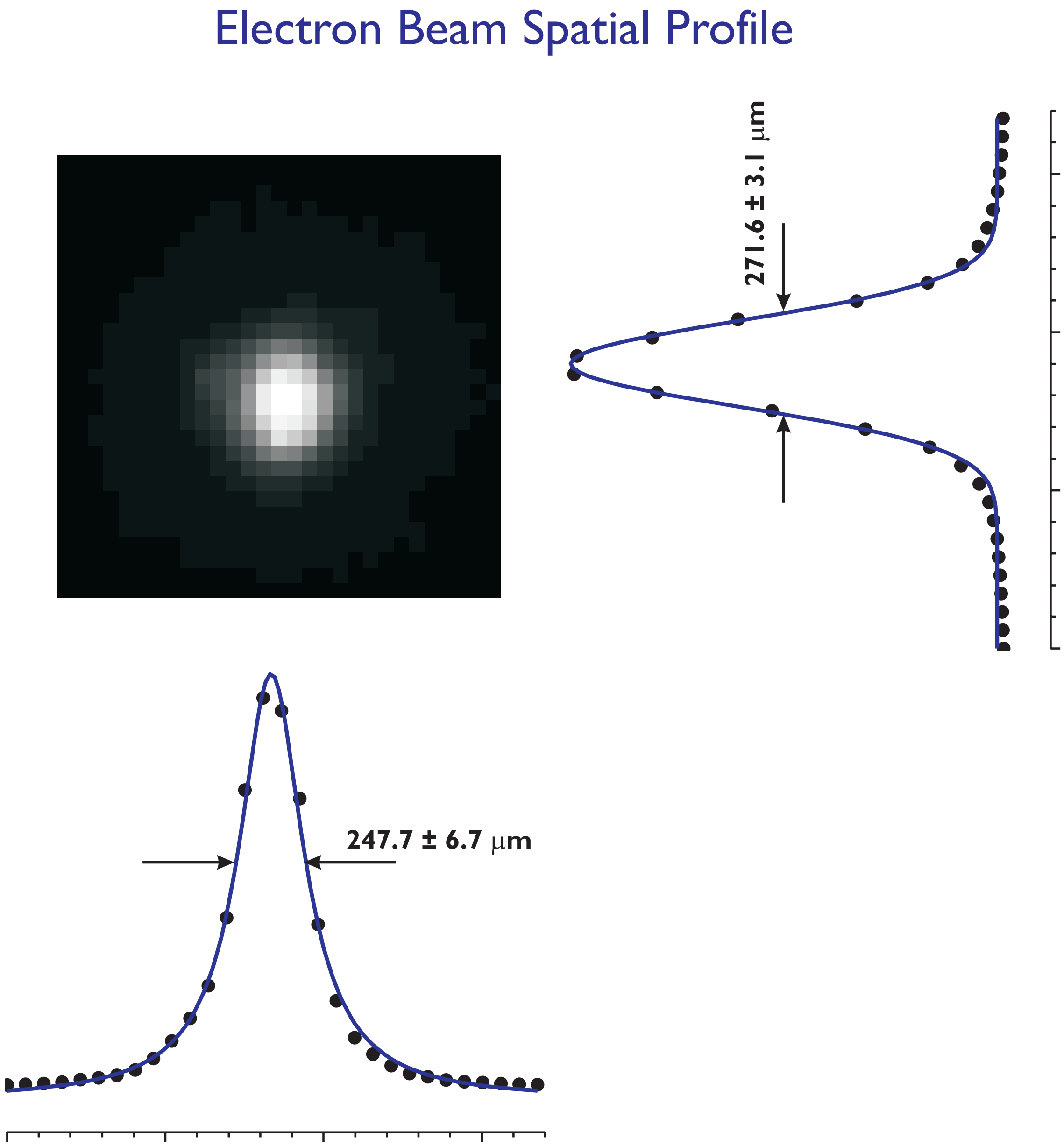

Figure 4-2. Typical X-Y profile of the nearly circular electron beam comprising ~4 ps pulses with ~25000 electrons/pulse. The image intensifier gain is 775V.

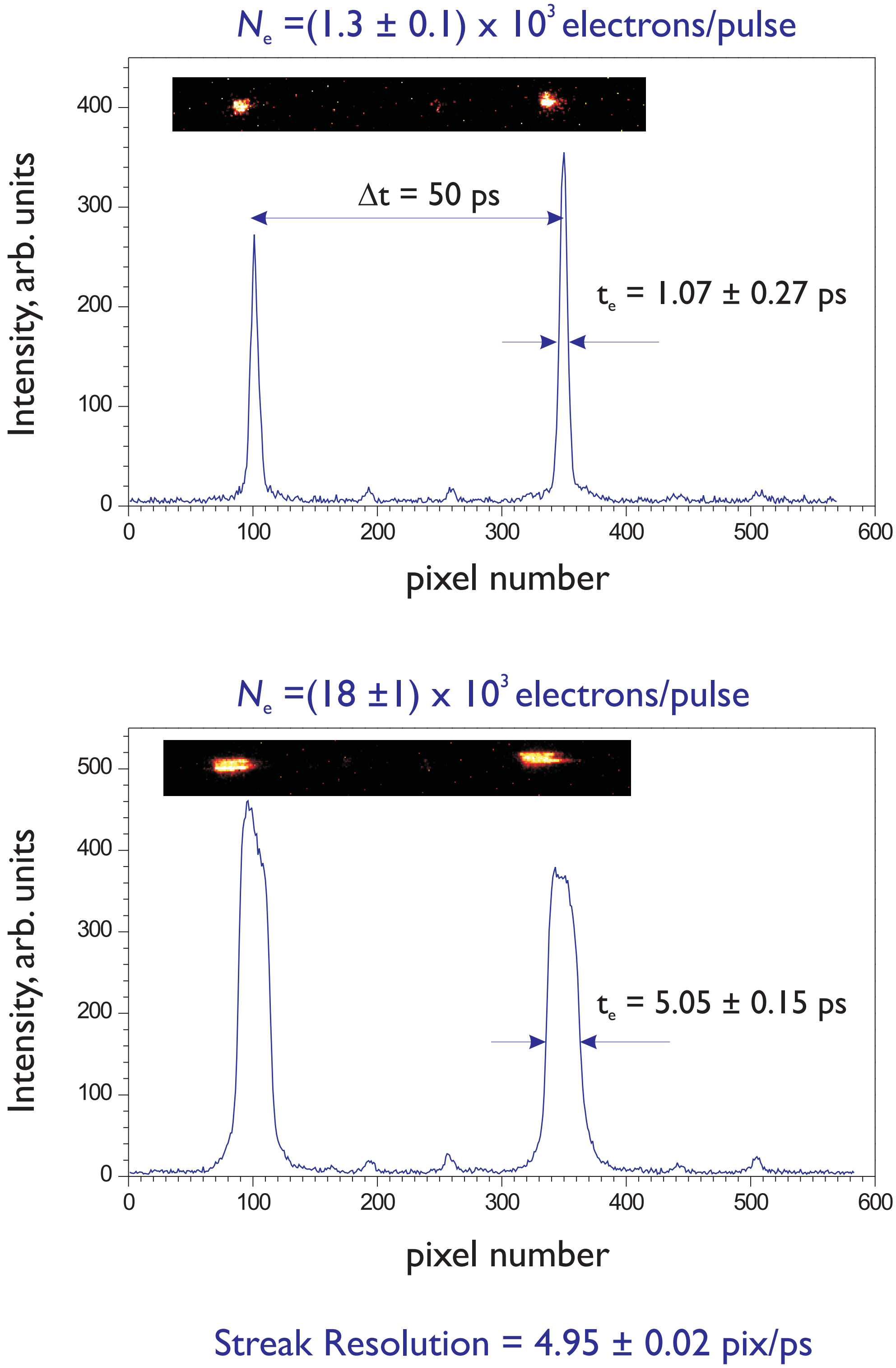

Figure 4-3. Results of an *in situ* streaking experiment showing ultrafast precision for electron pulse measurement in UED-3. The images of the streaked electron pulses separated by 50 ps are shown above the peaks of their respective profiles.

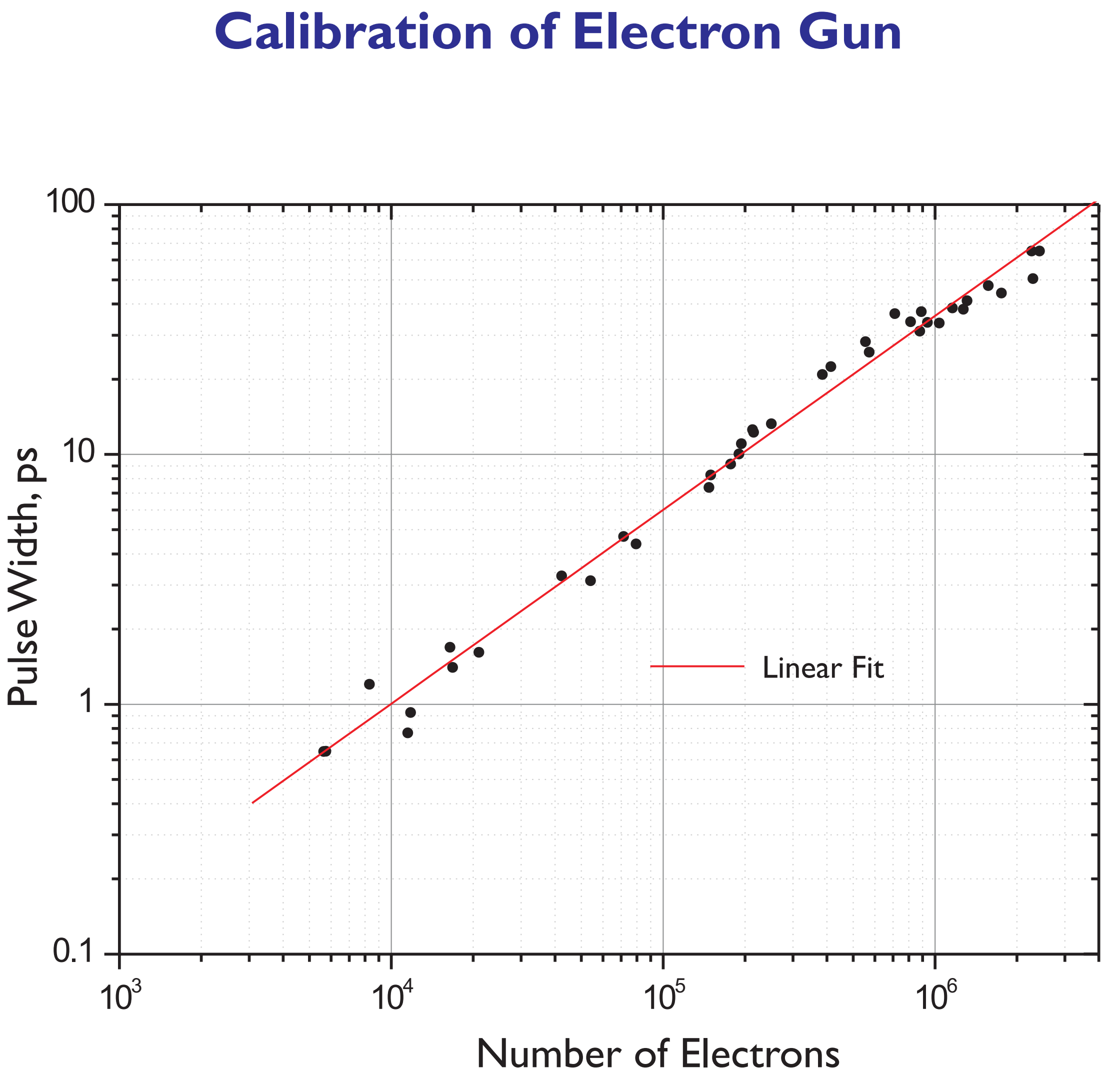

Figure 4-4. Calibration of electron pulse width as a function of the number of electrons per pulse.

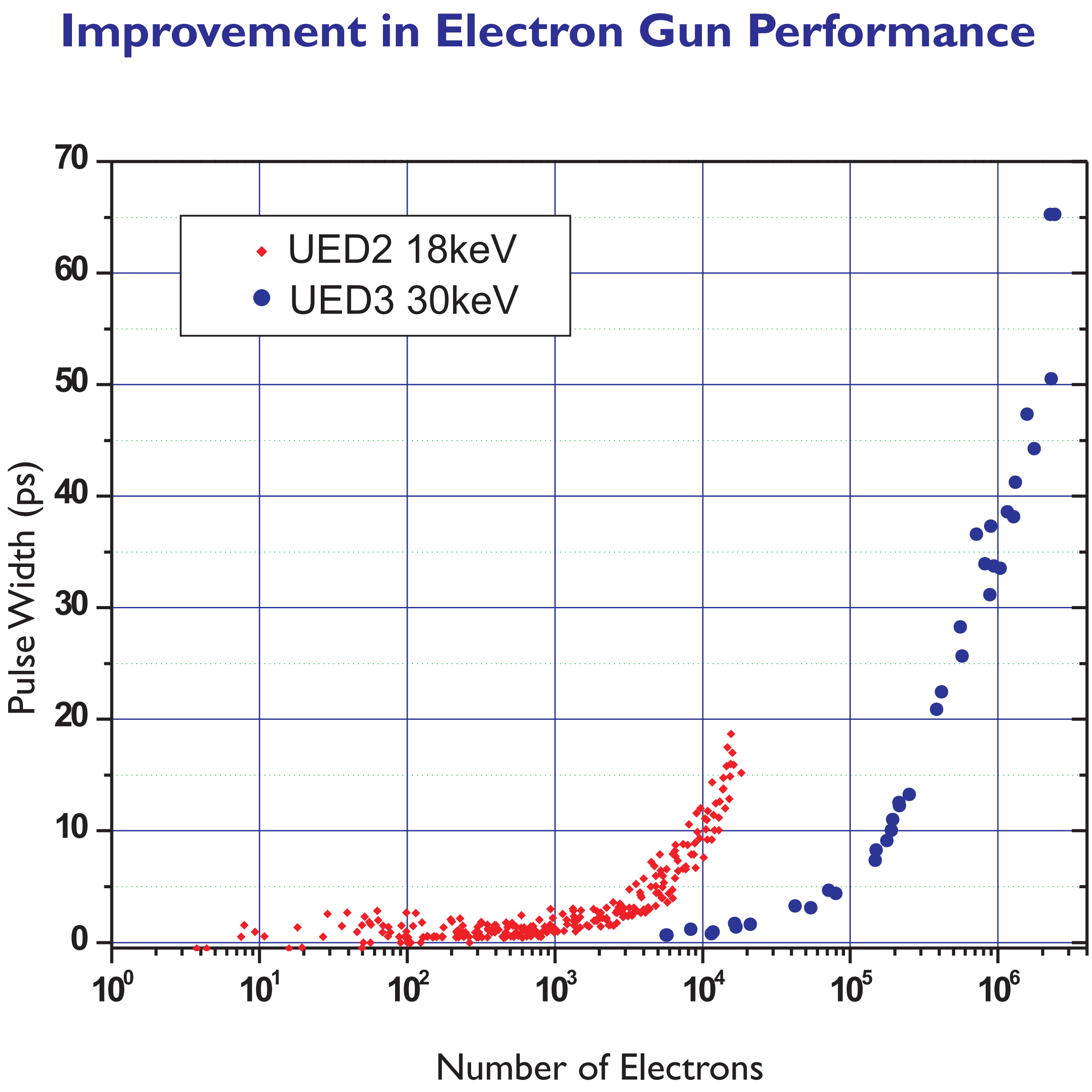

Improvement in Electron Gun Performance

Figure 4-5. Measured electron pulse widths as a function of the number of electrons. The blue curve (UED-3) shows more than an order-of-magnitude improvement in the electron gun performance in comparison to the red curve (UED-2).

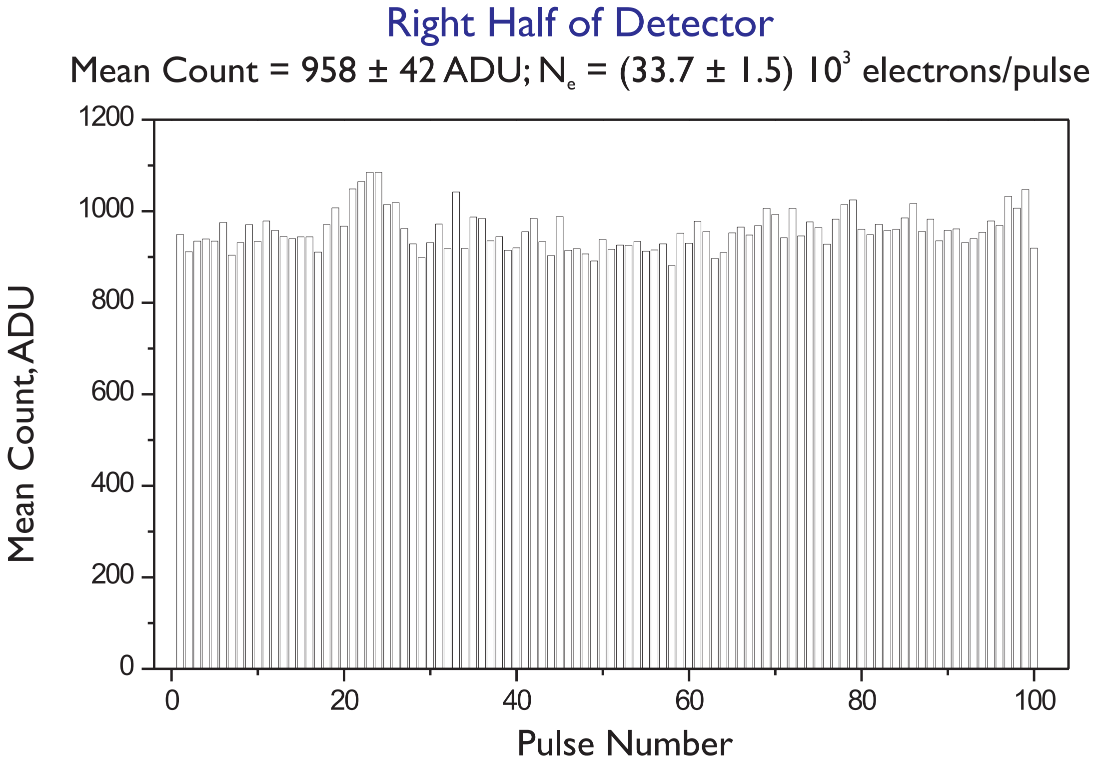

Right Half of Detector

Mean Count = 958 ± 42 ADU; N_e = (33.7 ± 1.5) 10^3 electrons/pulse

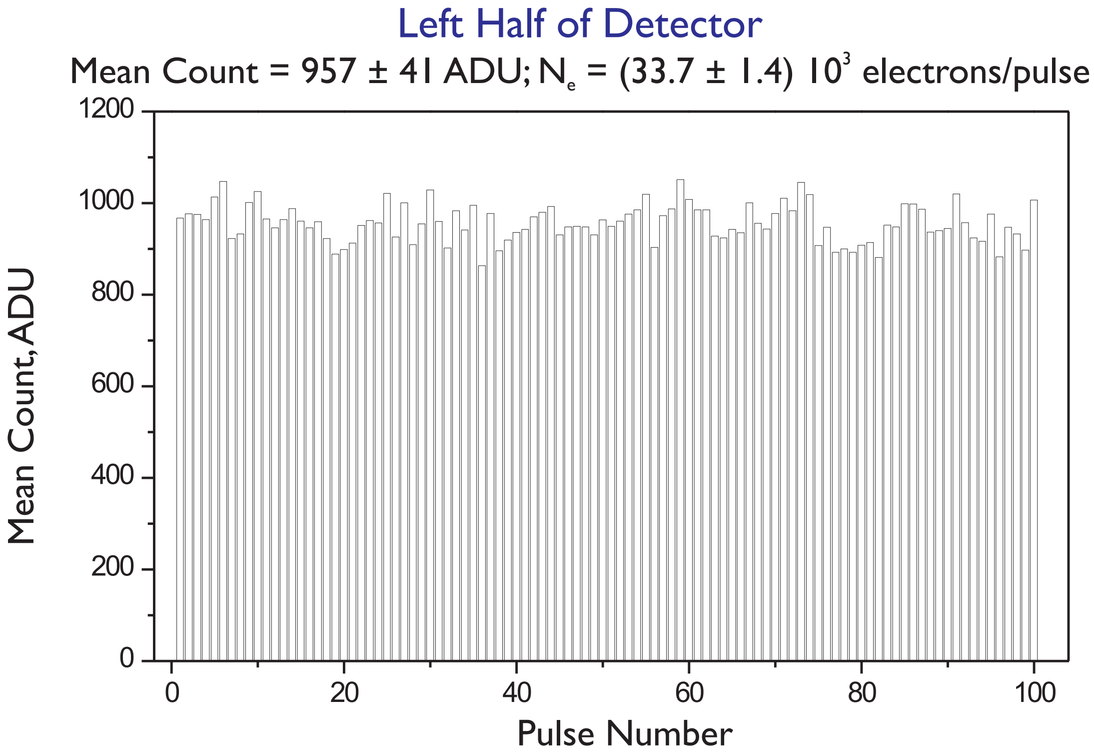

Left Half of Detector

Mean Count = 957 ± 41 ADU; N_e = (33.7 ± 1.4) 10^3 electrons/pulse

Figure 4-6. Pulse-to-pulse stability of the electron gun measured for 100 pulses on both sides of the detector. The measured statistics indicates the low variation in the average number of electrons/pulse.

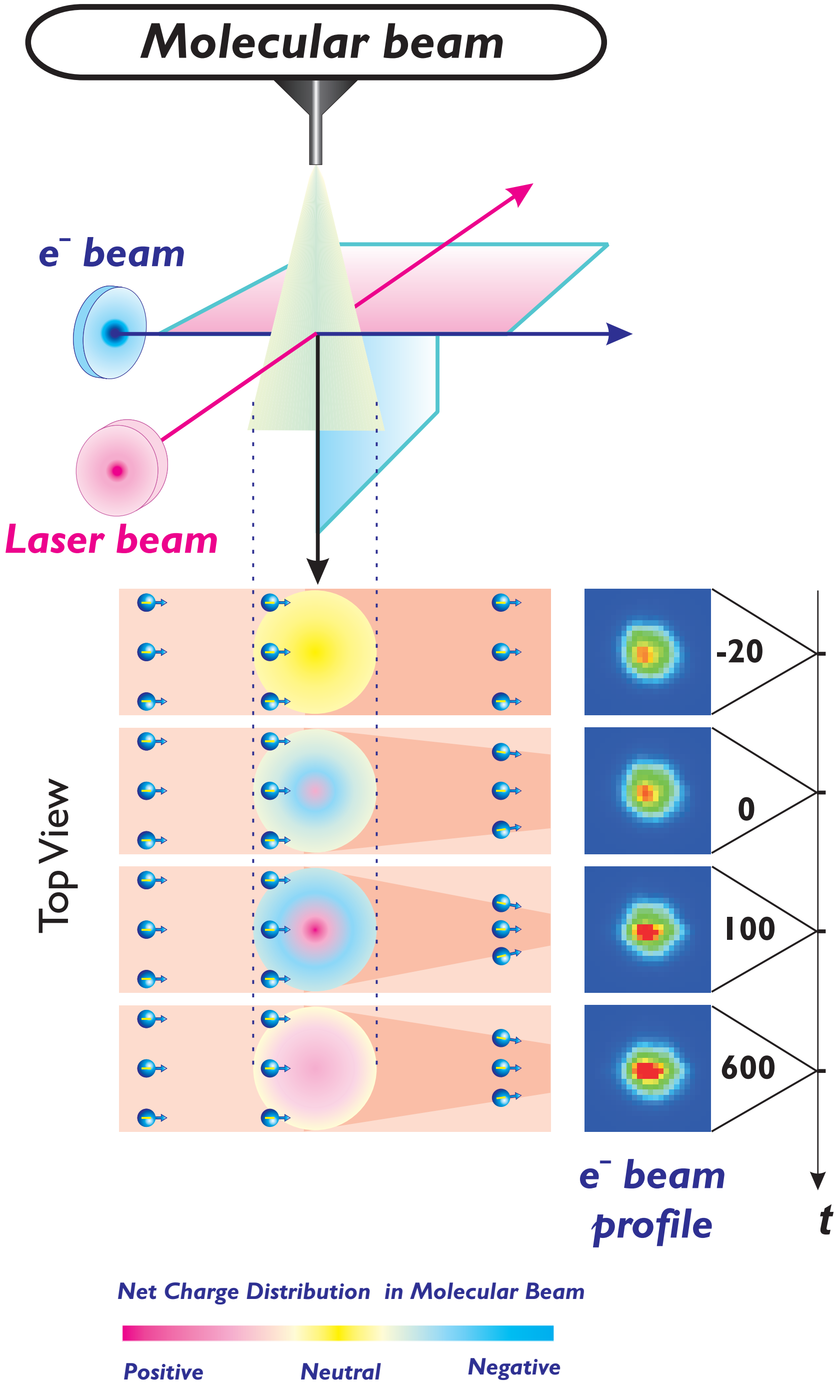

Figure 4-7. Schematic of the lensing experiment to determine *in situ* the zero-of-time. (*Top*) Excitation laser is incident on the molecular beam. (*Bottom*) Sequence of ionization-induced lensing. Excitation laser ionizes molecules within the sample through multiphoton absorption. The nascent electrons (depicted as a light blue cloud) exit the interaction region within picoseconds, while the positive ions (shown as a pink cloud) remain behind. The incident electron beam (shown as dark blue circles) is deflected by the resulting positively-charged ion lens, and the altered beam shape is detected on the CCD.

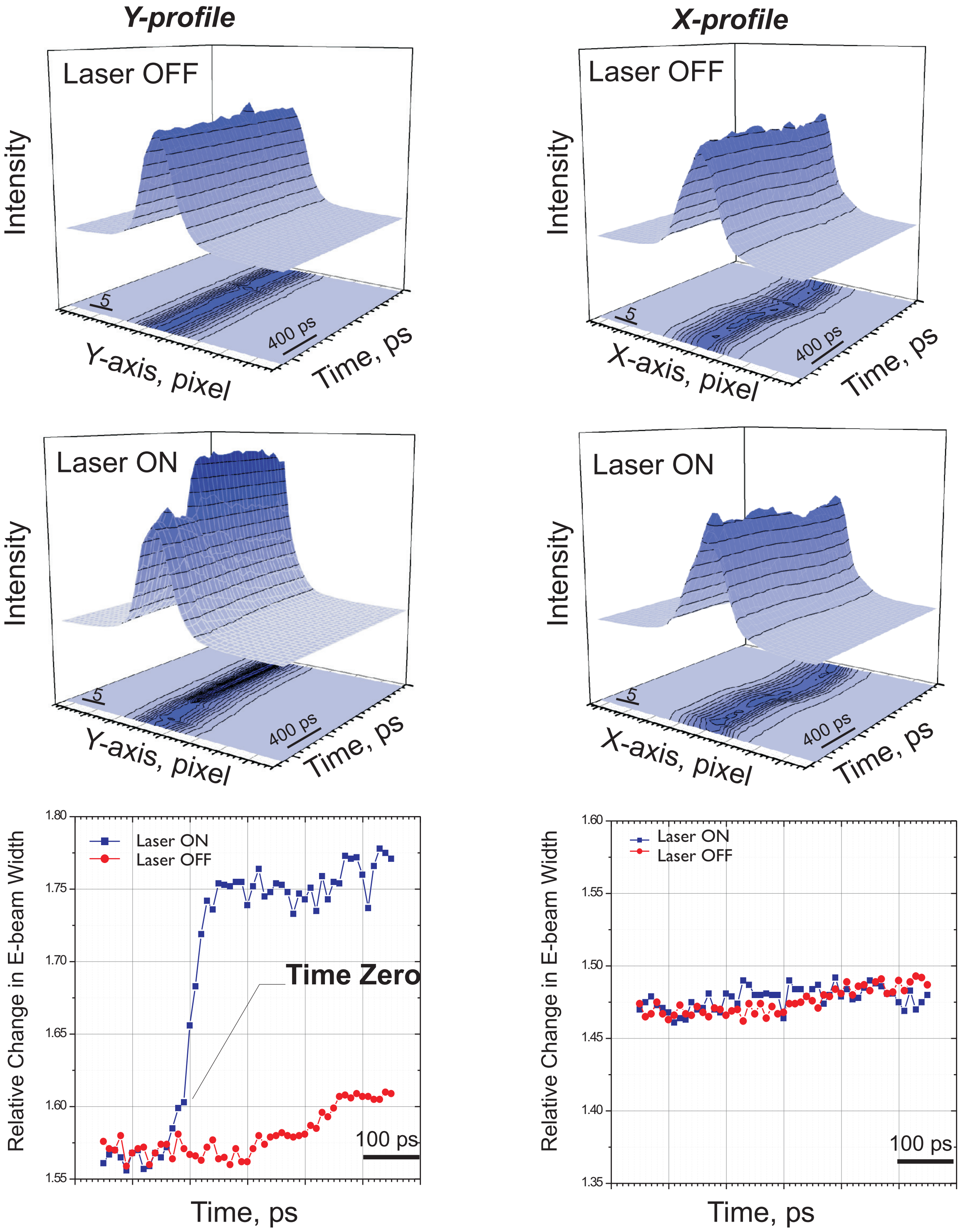

Figure 4-8. Photoionization-induced 'lensing' effect for measuring zero-of-time. A molecular beam of CF_3I was used. Left panel shows the vertical profile of the electron beam while the right panel shows the horizontal profile in absence (*top*) and presence (*middle*) of the laser. The *bottom* panel shows the variation of the fwhm of the electron beam profile as a function of the relative delay between the laser and electron pulses.

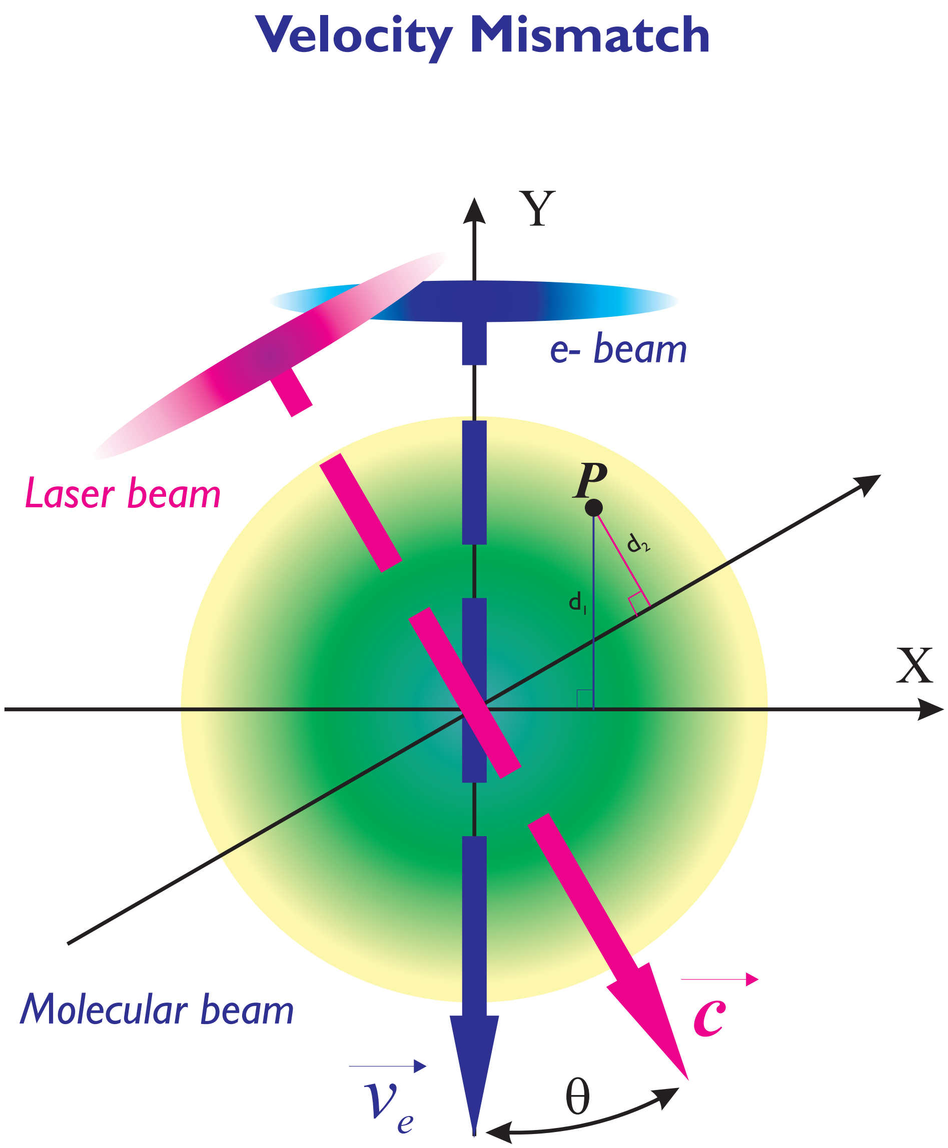

Figure 4-9. Geometry of a crossed-beam experiment. The trajectories of the laser and electron beams intersect at angle θ within the center of a molecular beam. The molecular beam flow is normal to the page, and a cross section of the beam is represented by the shaded coincident circles. If time zero is defined at the origin, then a molecule at point P observes a time delay t between the laser and electron pulses of $d_1/v_e - d_2/c$.

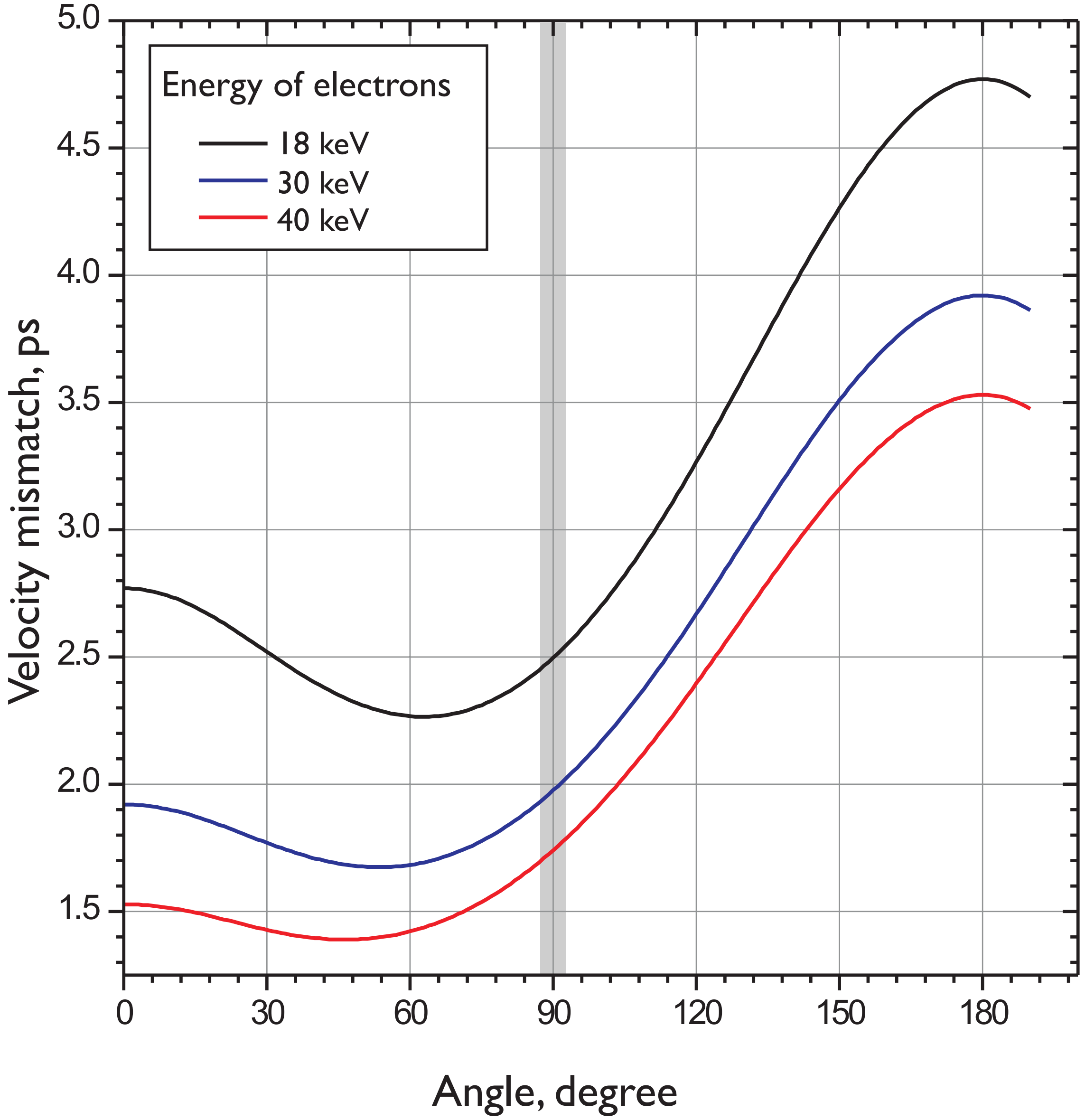

Molecular beam diameter, $w_M = 300$ μm
Electron beam diameter, $w_e = 250$ μm
Laser beam diameter, $w_L = 250$ μm

Figure 4-10. Angular dependence of the temporal broadening due to velocity mismatch (see text).

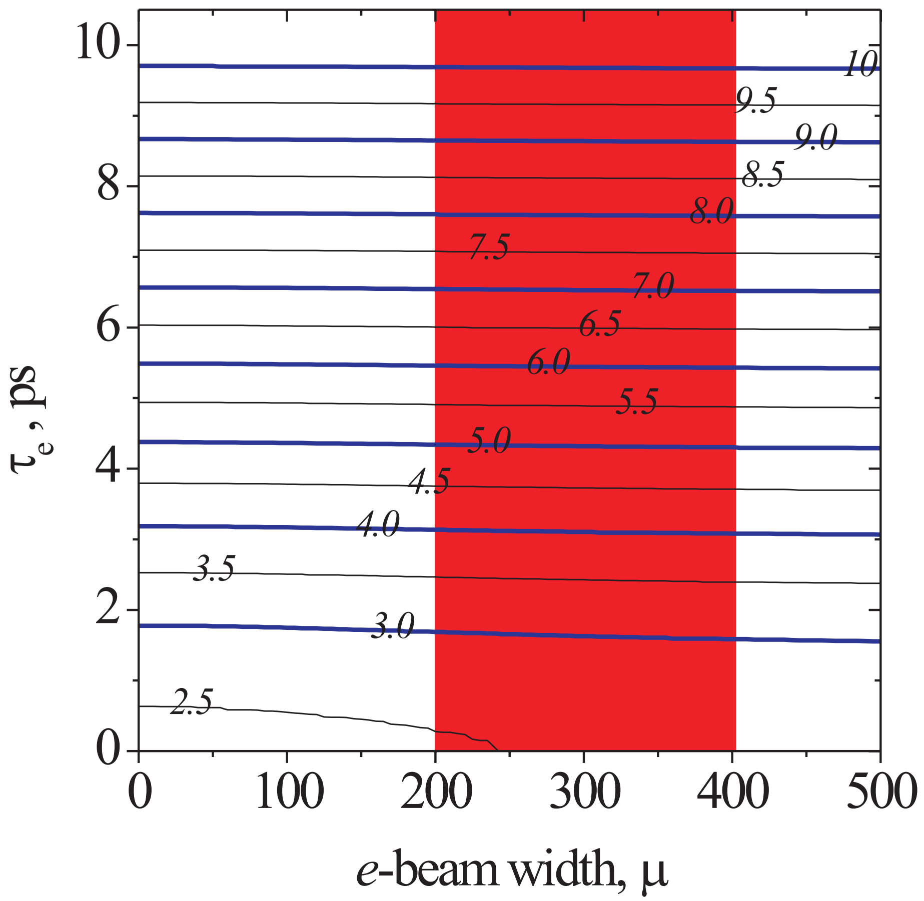

e-Gun Voltage, U = 30 kV
Molecular beam diameter, w_M = 300 μm
Laser beam diameter, w_M = 250 μm
Laser pulse width, t_L = 120 fs

Figure 4-11. Overall temporal resolution of UED-3 (including velocity mismatch) as a function of spatial and temporal width of the electron pulses.

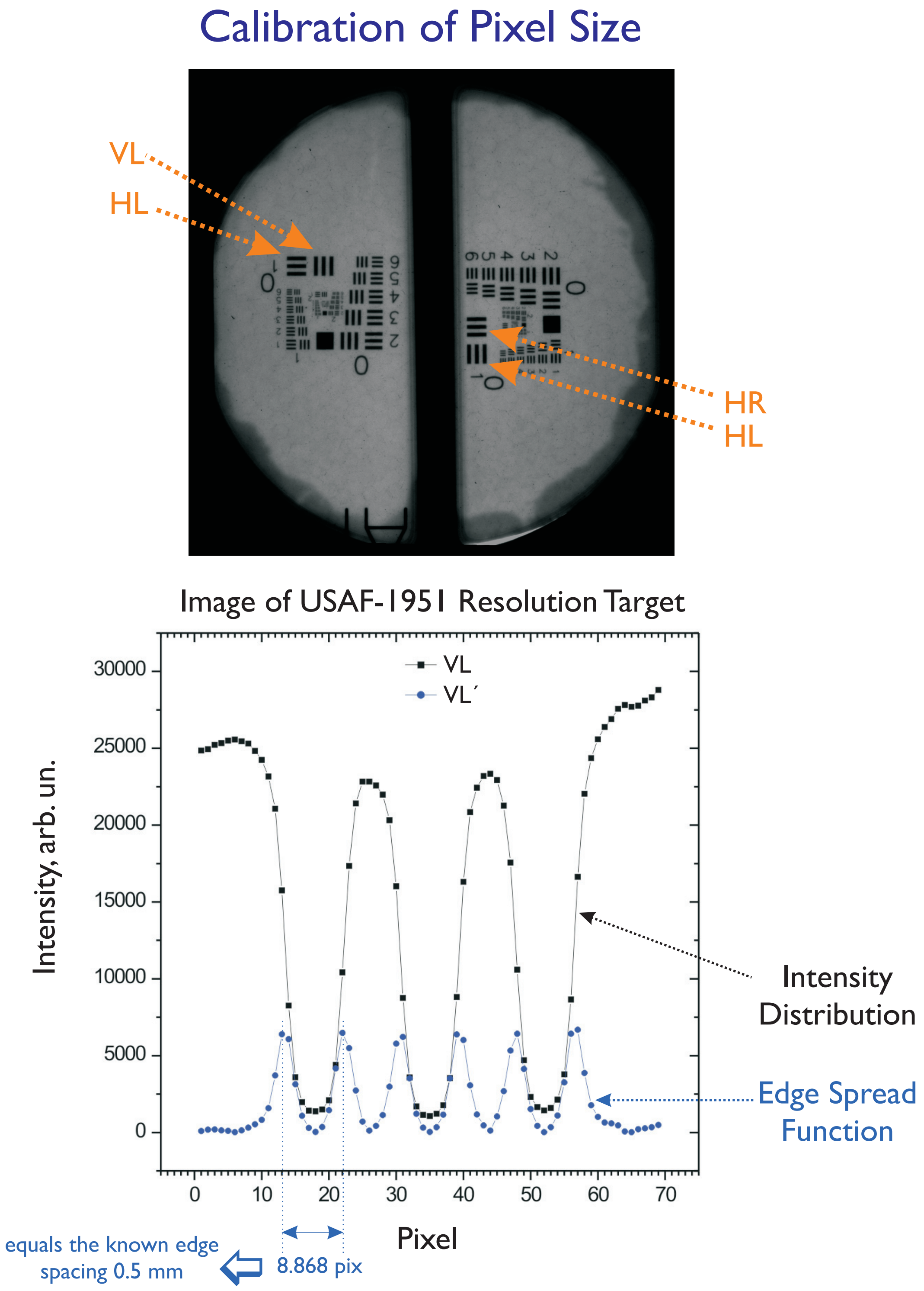

Figure 4-12. Calibration of the pixel size on the phosphor screen using Group 0, Element 1 of the USAF-1951 resolution target. The intensity distribution of the image is shown, the derivative of which gives the edge spread function. The peaks correspond to edges of the bar target, and hence, the peak spacing in pixels should correspond to the known edge spacing (0.5 mm).

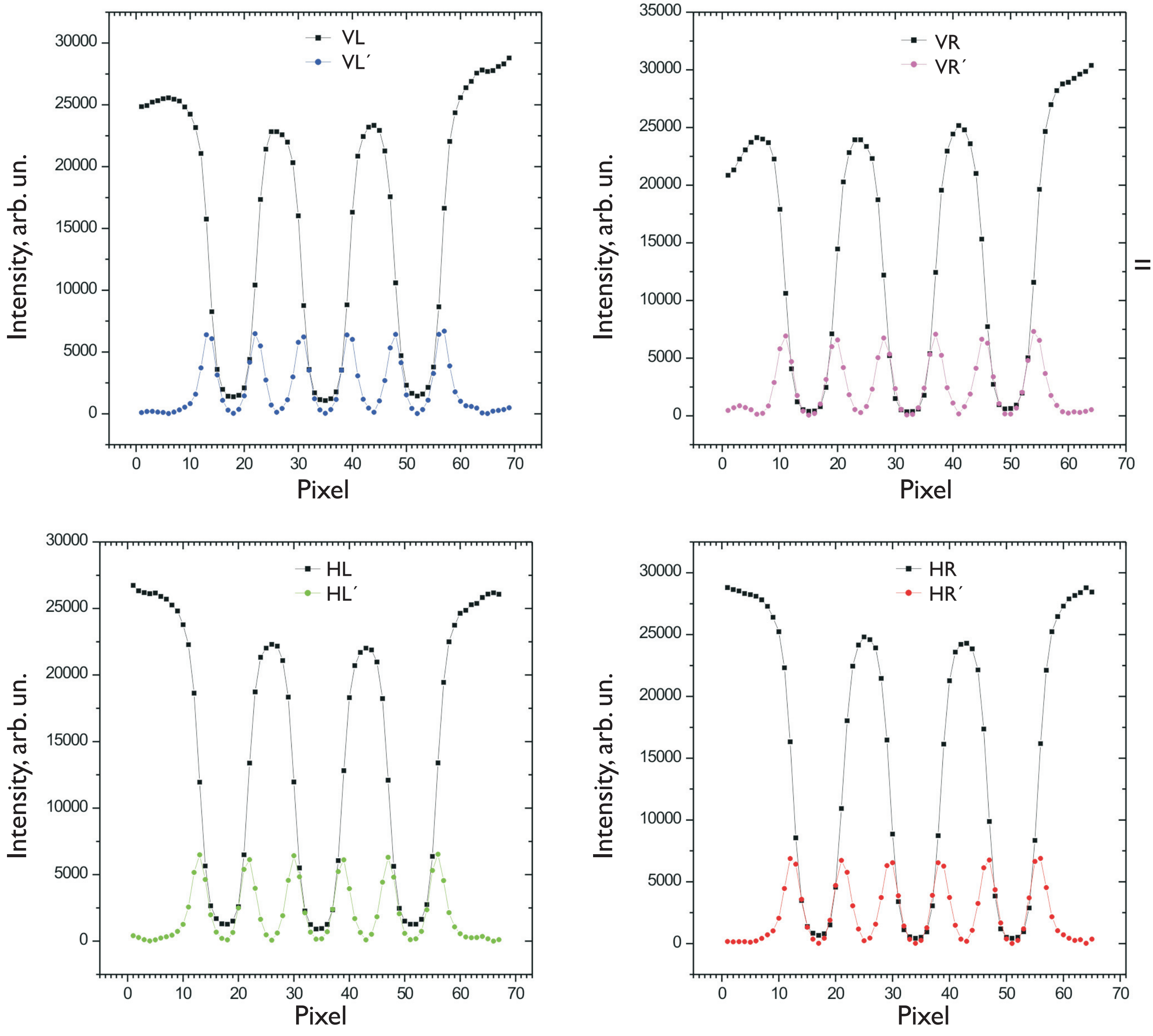

Mean Pixel Size
= 57.8 ± 2.12 μm/pix

Mean fwhm of ESF
= 161 ± 7 μm
~ 2.78 pix

Figure 4-13. Determination of mean pixel size on the phosphor screen. Shown are all measurements over the 4 elements – VL, HL, VR and HR – described in Fig. 4-12.

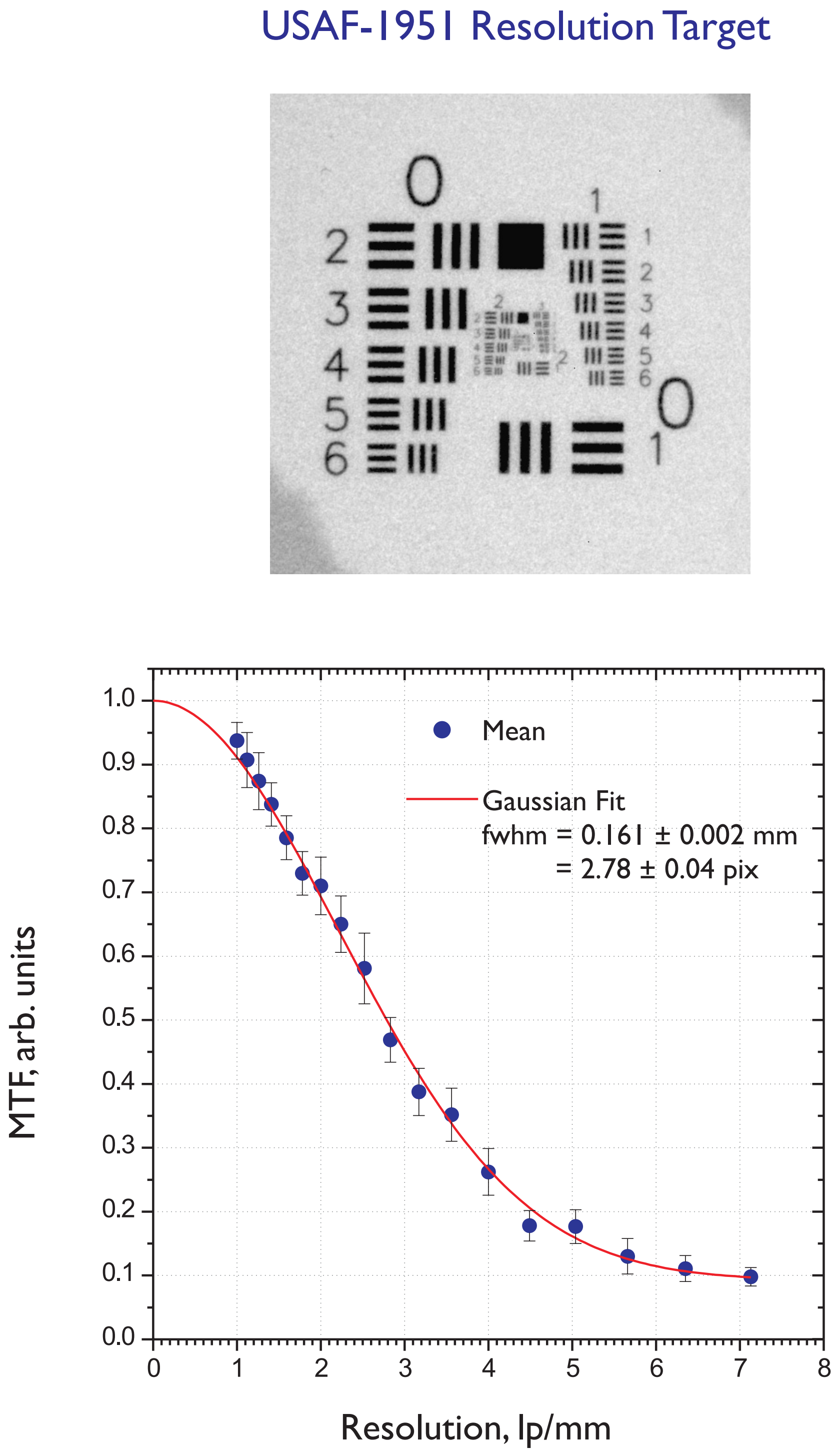

Figure 4-14. Modulation Transfer Function (MTF) for the ICCD camera. The plot indicates that the spatial resolution is 6.5 lp/mm. Shown on top is the USAF-1951 resolution target used for calibration of the imaging system. From the Gaussian fit to the MTF, the width of the point spread function is estimated to be ~ 2.78 pix.

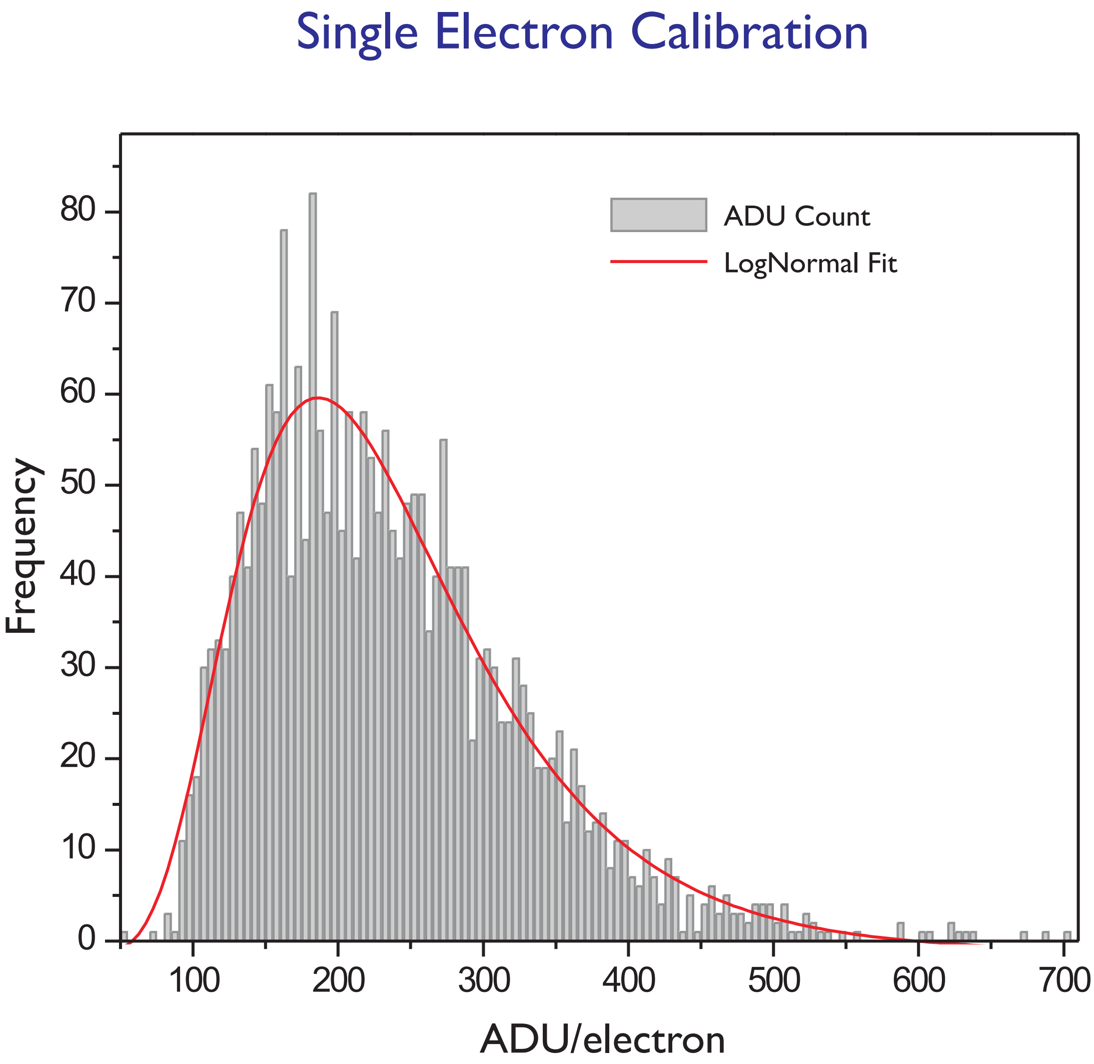

Image Intensifier Gain = 875 V
Phosphor = P-47
Mean ADU/electron = 186.3 ± 1.9

Figure 4-15. Calibration of single electron events on the detector with the P-47 phosphor screen at an image intensifier gain of 875 V.

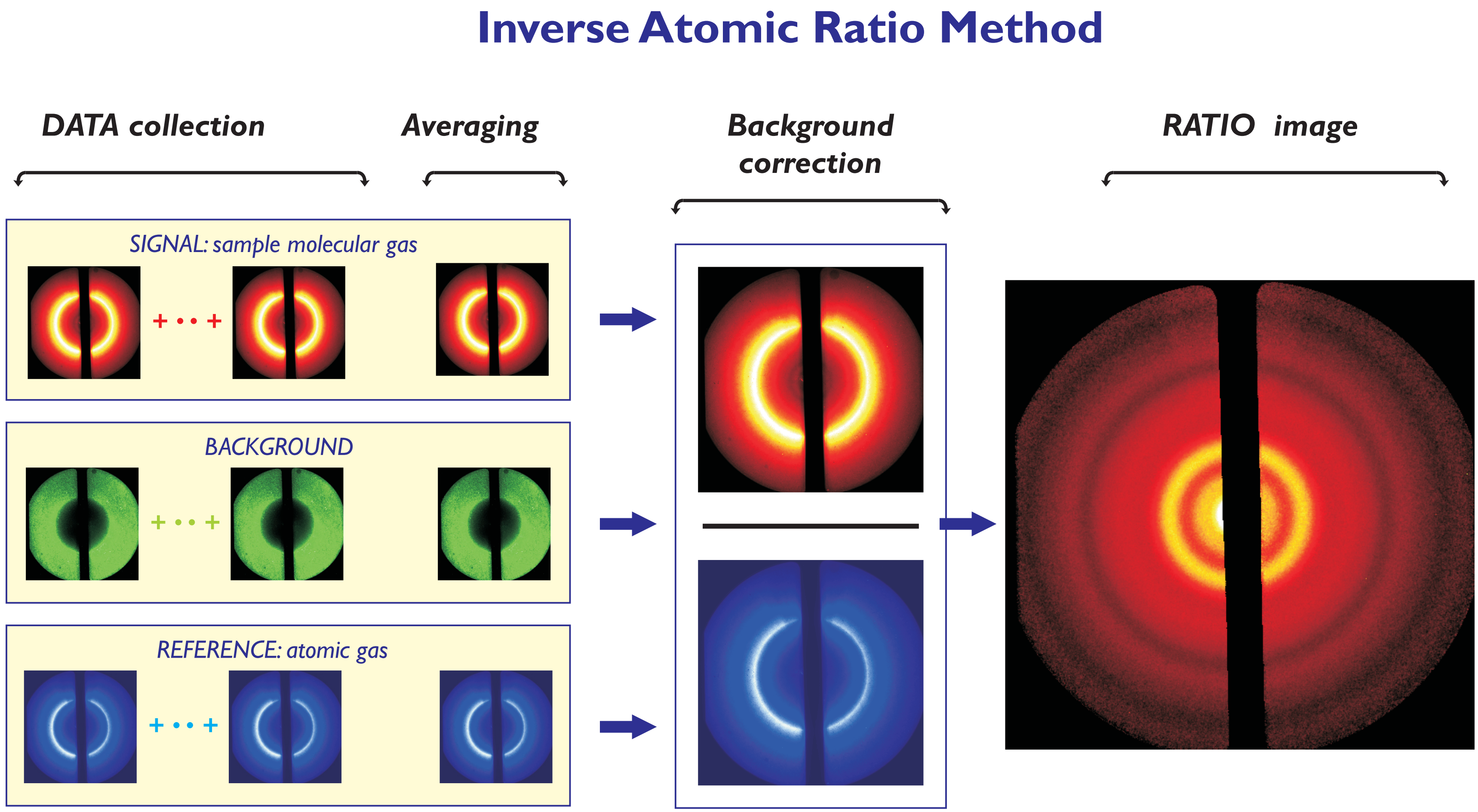

Figure 4-16. Schematic of inverse atomic ratio method that involves dividing the background-corrected signal image with that of a reference atomic gas (Xe) to account for the large incoherent atomic scattering, thereby recovering the coherent molecular scattering (manifested as rings in the 2D image).

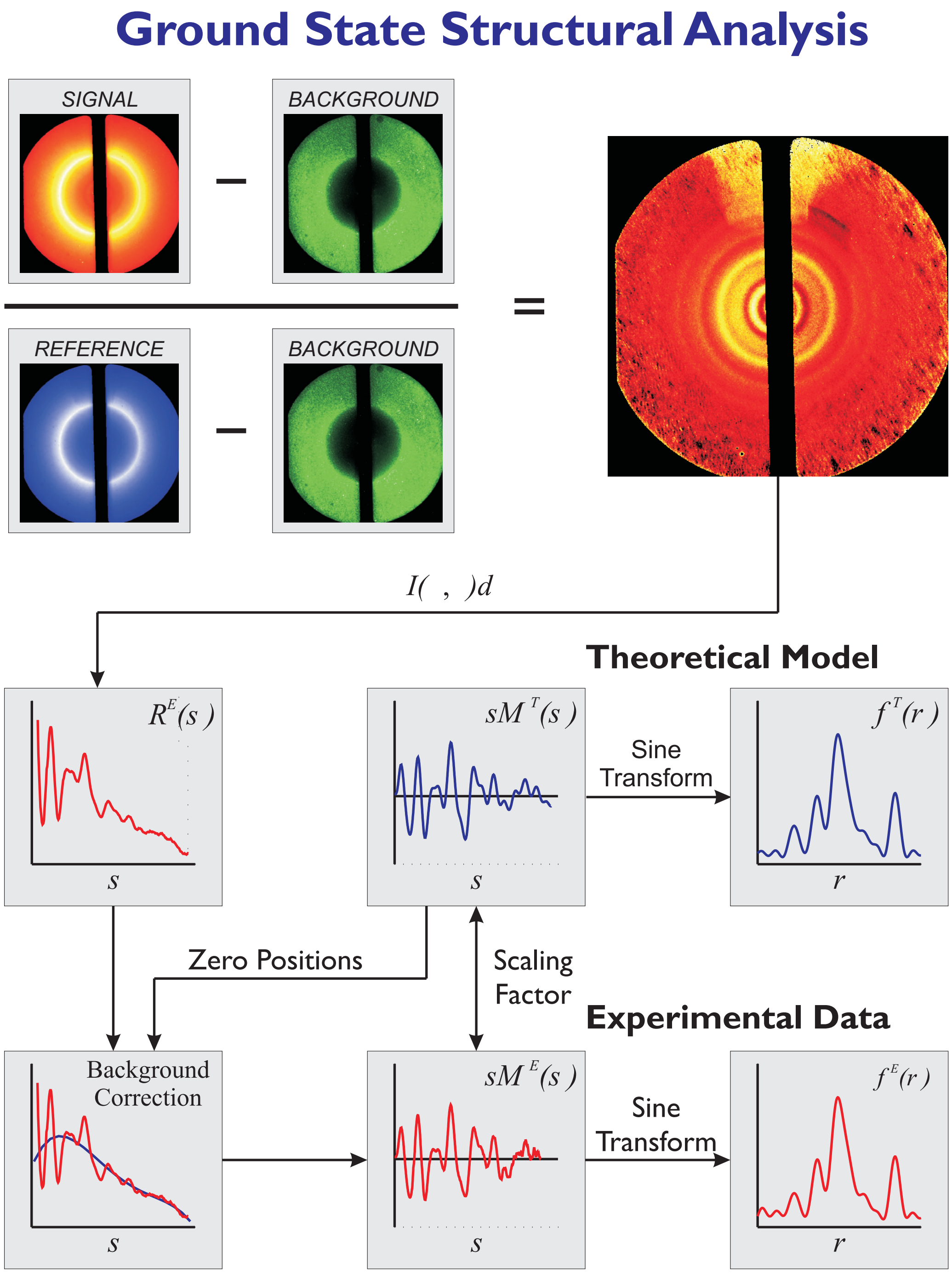

Figure 4-17. Schematic of the processing procedure for 2-D diffraction images and ground-state data analysis. Subtraction of the background image and division by the reference gas image yields a 2-D "ratio" image that clearly shows the rings of the molecular scattering signal. Following radial averaging of the ratio image, the unwanted background signal is subtracted from the 1-D curve to give the desired *sM*(*s*) curve, which can be compared with theoretical curves generated with iteratively refined structural parameters describing a given molecular species; the corresponding *f*(*r*) curves are obtained via sine transform.

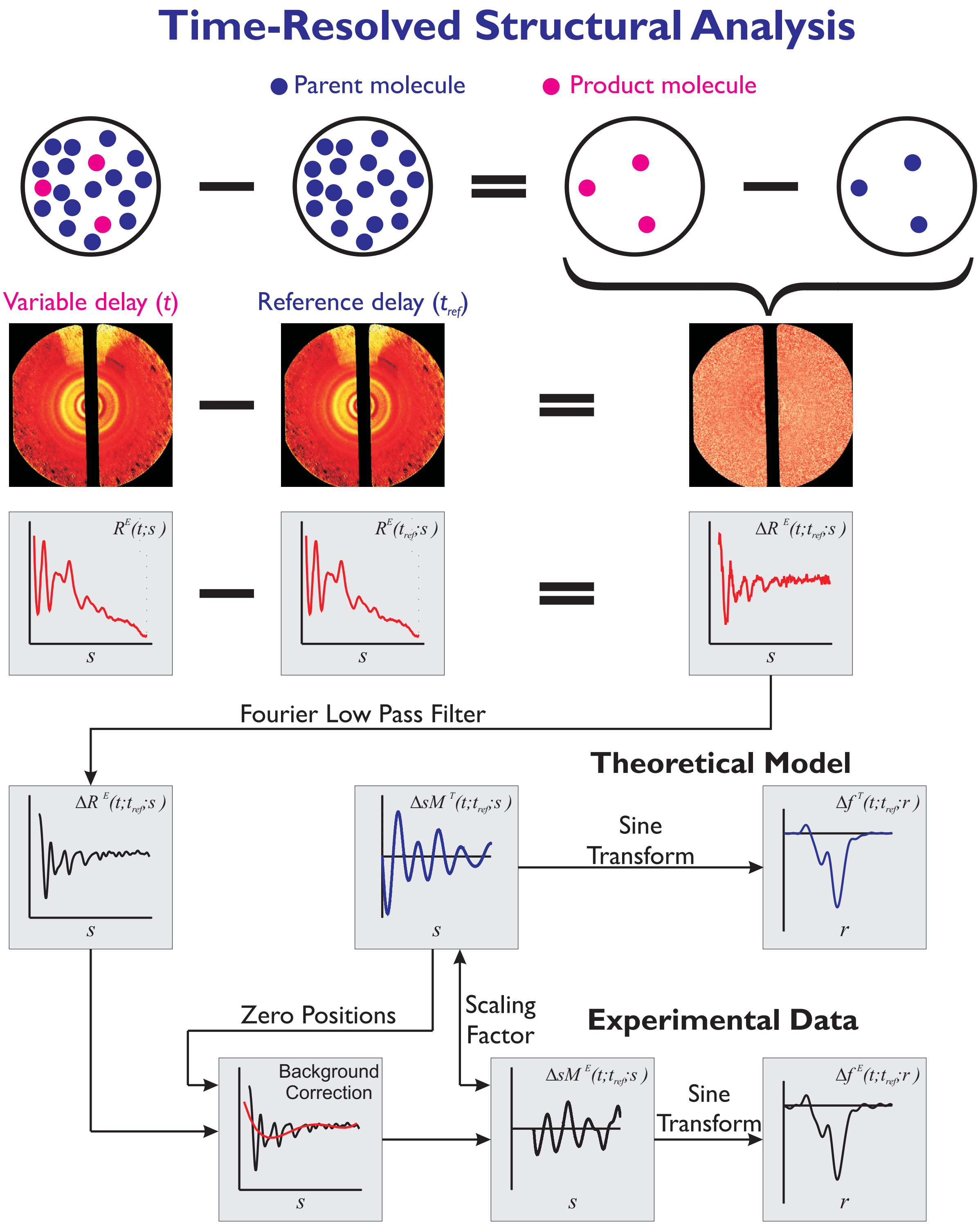

Figure 4-18. Schematic of the diffraction-difference analysis procedure for time-resolved experiments. The difference signal reflects only contributions from structural changes within the molecules. After Fourier filtering and background subtraction, information regarding the evolving structures can be obtained from the experimental $\Delta sM(s)$ curves.

e-Beam Divergence

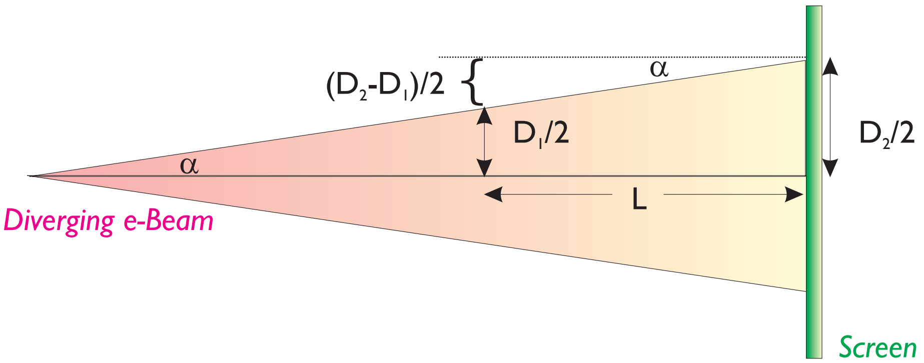

$$\mathrm{Div} = \mathrm{atan}\,((D_2-D_1)/2L)$$

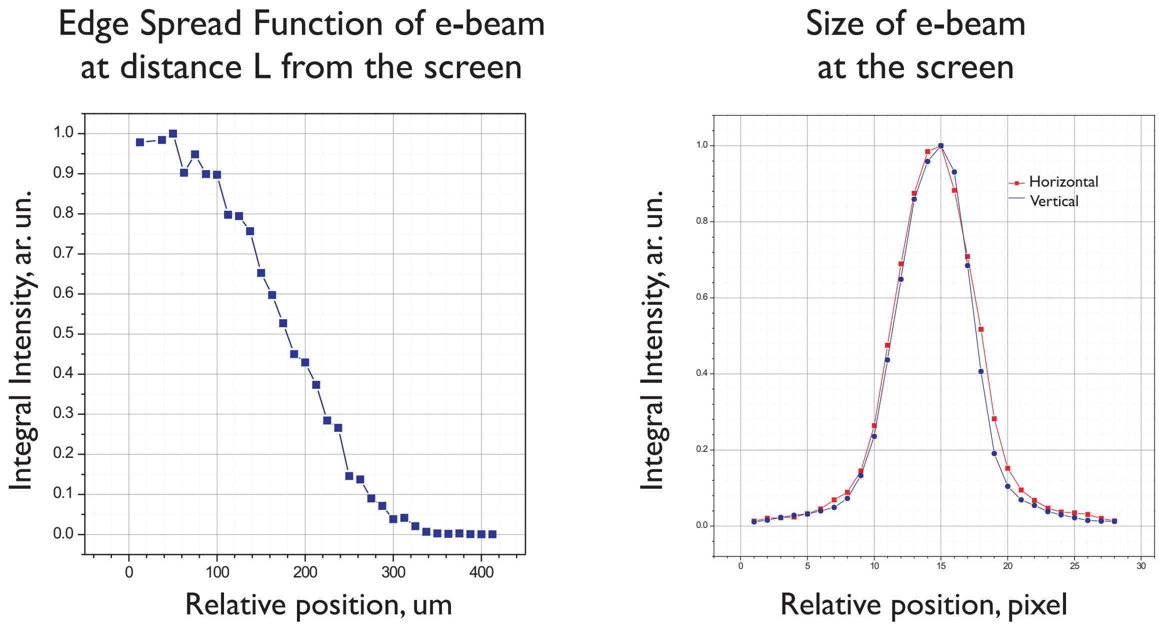
Edge Spread Function of e-beam at distance L from the screen

Size of e-beam at the screen

D_1(fwhm) = 261.8 ± 7.5 um

Vertical Size = 6.26 ± 0.11 pix

D_2 (fwhm) = 361.9 ± 15.5 um

Div = 0.35 mrad

Figure 4-19. Divergence of the electron beam. The edge spread function is measured by introducing a secondary Al target into the path of the e-beam at a distance of L = 143 mm from the phosphor screen and with steps of 0.125 mm. The resultant integral intensity measured on the screen is plotted against the position of the Al edge.